chemosensors

Review

Self-Assembled Plasmonic Interfaces for Wearable SERS: From Substrate Fabrication Toward Online Biofluid Sensing

Huicong Cao [1], Xinhao Zhuang [2,3], Guixian Zhu [1,4,*], Taotao Mu [1] and Yuan Ma [2,3,*]

[1] School of Instrument Science and Optoelectronic Engineering, Beijing Information Science and Technology University, Beijing 100192, China; 2025020306@bistu.edu.cn (H.C.); 20172088@bistu.edu.cn (T.M.)
[2] State Key Laboratory of Tribology in Advanced Equipment, Tsinghua University, Beijing 100084, China; zhuangxh25@mails.tsinghua.edu.cn
[3] Department of Mechanical Engineering, Tsinghua University, Beijing 100084, China
[4] Key Laboratory of Modern Optoelectronic Measurement Technology in Mechanical Industry, Beijing Information Science and Technology University, Beijing 102206, China
* Correspondence: zhuguixian@bistu.edu.cn (G.Z.); yuanma@tsinghua.edu.cn (Y.M.)

Abstract

Wearable health monitoring is expanding from physical signals, such as heart rate and body temperature, to molecular information at body interfaces and in biofluids. Raman spectroscopy provides chemically specific vibrational fingerprints and supports label-free molecular analysis. Surface-enhanced Raman scattering (SERS) further improves sensitivity through plasmonic enhancement, enabling analysis of low-abundance biomarkers. For wearable sensing, SERS-active structures must provide reliable hotspots, integrate with flexible or three-dimensional supports, and remain compatible with biofluid sampling. Self-assembly offers a bottom-up route to generate nanoscale interparticle gaps and integrate plasmonic structures with diverse supports. Existing reviews have mainly focused on biomedical SERS, flexible SERS substrates, or nanoparticle assembly, while links between self-assembly routes, biofluid sampling, and wearable integration have received less systematic attention. This review summarizes recent progress in self-assembled plasmonic structures for wearable SERS. Reported strategies are classified as fluid-interface, evaporation-induced, and template-assisted self-assembly according to the dominant assembly process and spatial constraints. Representative studies involving sweat, interstitial fluid, tears, and wound exudate are compared across biofluid-sensing scenarios. Finally, we discuss the stability of the effective sensing area under on-body conditions and quantitative validation in real biofluids.

Keywords: wearable sensing; surface-enhanced Raman scattering; self-assembly; flexible plasmonic structures; biofluid analysis; online monitoring

Check for updates

Received: 18 September 2026
Revised: 8 October 2026
Accepted: 12 October 2026
Published: 15 October 2026

Copyright: © 2026 by the authors. Licensee MDPI, Basel, Switzerland. This article is an open access article distributed under the terms and conditions of the Creative Commons Attribution (CC BY) license.

1. Introduction

In recent years, wearable health monitoring has expanded beyond physical signals such as heart rate, body temperature, and physical activity to the analysis of molecular information that reflects metabolic and physiological states [1–4]. Compared with intermittent sampling and ex vivo analysis, wearable biochemical sensing enables direct access to biofluids at the body interface and subsequent signal readout, allowing repeated in situ biomarker measurements with minimal tissue disruption [1,5,6]. Sweat, tears, skin interstitial fluid (ISF), and wound exudate are representative biofluids for such applications. Sweat and tears can be collected noninvasively, ISF can be accessed minimally invasively

using approaches such as microneedles, and wound exudate can be used to assess local wound status [5,7–9]. These biofluids differ substantially in sample volume, collection method, and matrix composition, which in turn affect sample transport to the sensing region and subsequent signal acquisition.

Electrochemical, colorimetric, and fluorescence-based methods have been widely used in wearable biochemical sensing and offer rapid response, ease of integration, and real-time readout [10–12]. However, their signals typically manifest as changes in current, potential, color, or fluorescence intensity, while target recognition generally depends on specific probes, enzymatic reactions, or molecular recognition systems [10–12]. In contrast, Raman spectroscopy provides chemically specific vibrational fingerprints and supports label-free molecular analysis [13,14]. A single spectral acquisition can capture multiple molecular features simultaneously, supporting multicomponent analysis in complex biofluids. However, the intrinsically small Raman scattering cross-section limits the detection of low-abundance biomarkers by conventional Raman spectroscopy [14–18]. Surface-enhanced Raman scattering (SERS) substantially improves Raman sensitivity primarily through localized electromagnetic-field enhancement generated by metallic nanostructures, with an additional contribution from chemical enhancement [14–18]. In addition to particle size, morphology, orientation, and interparticle spacing, analyte transport to and adsorption at high-enhancement regions also affect the SERS response.

Owing to these characteristics, SERS has been extensively investigated in biomedical analysis, including early cancer detection, infectious-disease-related analysis, and the detection of clinically relevant biomarkers [19–22]. Beyond the body-interface biofluids emphasized in wearable sensing, SERS has also been applied to whole blood, plasma or serum, saliva, and urine [19–25]. Representative applications include therapeutic drug monitoring, pathogen identification, protein biomarker analysis, and disease-associated spectral profiling. These studies illustrate the broader biomedical scope of SERS. In this review, however, we focus on sweat, interstitial fluid, tears, and wound exudate because these biofluids can be coupled more directly with wearable or minimally invasive sampling interfaces.

When incorporated into wearable platforms such as flexible supports, microfluidic structures, or microneedles, SERS substrates are additionally exposed to mechanical deformation arising from bending, stretching, and microneedle insertion. Such deformation may perturb particle arrangement, interparticle spacing, and attachment, thereby altering hotspot configurations and the SERS response [26–30]. Periodic plasmonic architectures with well-defined feature dimensions, spacing, and periodicity can be fabricated using lithographic and template-based nanofabrication methods. Representative geometries include nanocone, nanopillar, nanodisk, nanohole, and nanopyramid arrays [31–34]. Electron-beam and related lithographic approaches offer precise structural control but often require sophisticated instrumentation and multistep processing [29,32,33], whereas nanosphere or colloidal templating provides a scalable route for some periodic geometries [31–34]. Direct deposition and coating are more readily applicable to flexible supports, although their ability to regulate particle organization and nanoscale gap formation is comparatively limited [26,27]. Achieving integration with flexible and three-dimensional supports while preserving stable SERS-active regions therefore remains an important challenge in wearable SERS substrate fabrication.

Self-assembly is a bottom-up approach to substrate fabrication [35–38]. Interparticle interactions, interfacial energy, capillary transport, solvent evaporation, and template confinement govern the migration and organization of plasmonic particles. These assembled structures are integrated with the final support through either film transfer or direct deposition [35,36,39]. Assembly routes differ in where hotspots form and in the structures they produce. The subsequent fixation of these structures on the support can further influ-

ence structural stability during wear. Existing reviews have focused mainly on biomedical SERS, flexible SERS substrates, or nanoparticle assembly [14,18,26–30,35,36]. However, systematic comparisons of their practical applications across different biofluid-sampling scenarios remain limited.

This review classifies the relevant self-assembly approaches into fluid-interface, evaporation-induced, and template-assisted self-assembly according to the dominant particle-assembly mechanism and mode of spatial confinement [40–42]. The three routes are compared in terms of structure formation and integration with supports, and their practical applications are discussed through representative studies involving sweat, interstitial fluid, tears, and wound exudate. Finally, the stability of the effective sensing area under on-body conditions and quantitative validation in real biofluids are discussed.

2. Self-Assembly Strategies and Wearable Integration of SERS Interfaces

Colloidal self-assembly is used to construct SERS-active nanoparticle arrangements and immobilize them on flexible or three-dimensional supports. According to the dominant process governing particle organization, the approaches discussed here are classified as fluid-interface, evaporation-induced, and template-assisted self-assembly, as schematically illustrated in Figure 1A–C. After assembly, the resulting plasmonic interfaces must remain accessible to the sampled biofluid and to the Raman excitation and collection path while being retained on the final support. The overall connection between biofluid sampling, the SERS-active wearable interface, and external optical readout is summarized in Figure 1D.

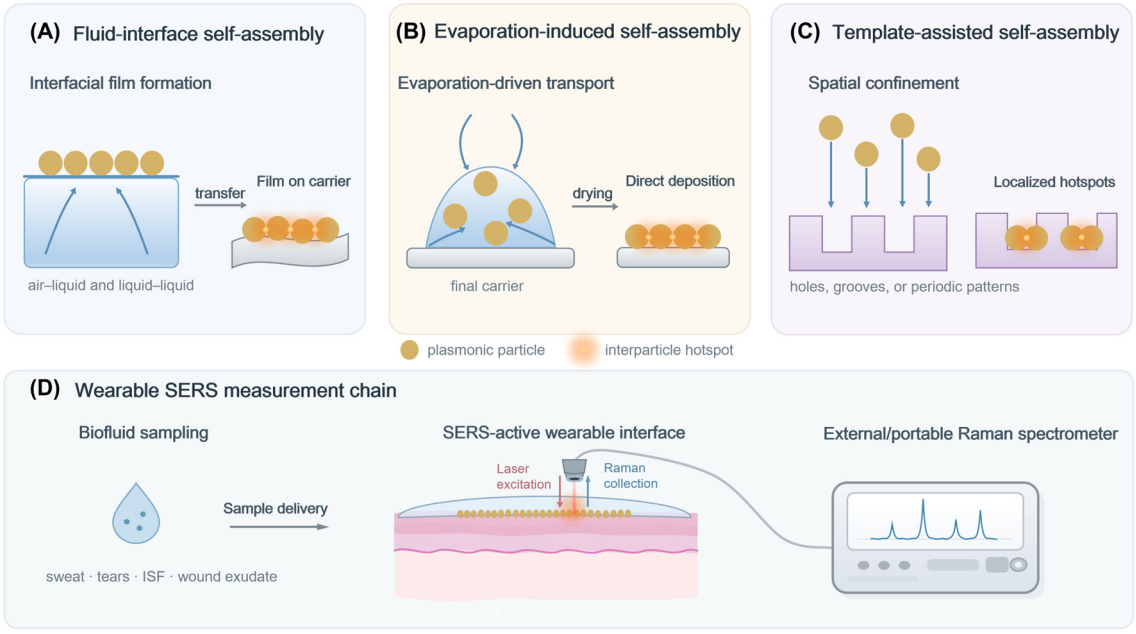


Figure 1. Schematic illustration of self-assembly strategies and wearable surface-enhanced Raman scattering (SERS) integration. (**A**) Fluid-interface self-assembly, in which particles form a film at an air–liquid or liquid–liquid interface before transfer to the final support. (**B**) Evaporation-induced self-assembly, in which particles are transported during drying and deposited directly onto the final support. (**C**) Template-assisted self-assembly, in which spatial confinement directs particles to predefined locations to form hotspots. (**D**) General measurement chain for wearable SERS, linking the sampling of sweat, tears, interstitial fluid (ISF), and wound exudate with the SERS-active interface, laser excitation, Raman signal collection, and an external or portable Raman spectrometer.

2.1. Fluid-Interface Self-Assembly

Random aggregation can generate localized hotspots with strong enhancement, but limited control over interparticle spacing and aggregate morphology often leads to

nonuniform hotspot distributions and SERS signals. Interfacial assembly exploits the two-dimensional confinement of liquid–liquid or air–liquid interfaces, where dispersed nanoparticles first assemble into continuous or quasi-continuous films before being transferred to the target support [43,44].

A central requirement for liquid–liquid interfacial assembly is to weaken colloidal stabilization while preserving particle migration and rearrangement along the interface [43–46]. Control primarily involves particle surface chemistry, interparticle interactions, and the dispersion medium. Alkanethiols increase particle hydrophobicity through Au–S bonding, whereas tetraalkylammonium salt promoters reduce electrostatic repulsion by ionic screening [45]. Cosolvents miscible with both phases, such as ethanol, reduce surface charge and colloidal stability, thereby promoting particle migration toward the interface [46].

Particle films formed at liquid–liquid interfaces can be converted into flexible SERS substrates by direct retrieval, transfer onto polymer supports, or in situ polymer curing [47,48]. Li and Chin assembled Ag nanocube arrays at a cyclohexane–water interface and immobilized the arrays on the surface of a newly formed polydimethylsiloxane (PDMS) membrane through in situ curing of the PDMS precursor, yielding a flexible substrate with a relative standard deviation (RSD) of about 12% [49]. Peng et al. transferred a self-assembled gold nanoparticle (AuNP) film from a water–toluene interface onto PDMS nanowrinkles. The nanowrinkled structure improved the substrate's adaptability to dynamic deformation and maintained stable SERS performance after repeated bending (Figure 2A) [50].

Air–liquid interfacial assembly can employ electrolyte screening, Langmuir–Blodgett compression, or evaporation-assisted particle supply to enrich nanoparticles at the open liquid surface and allow them to rearrange [43,51–54]. Once adsorbed, the particles are strongly confined normal to the interface but retain lateral mobility. The assembled films can then be retrieved and transferred onto target supports [13,51,55]. Different control strategies produce distinct film structures. Electrolyte screening promotes the formation of quasi-two-dimensional fractal Ag films [41]. Langmuir–Blodgett compression regulates the phase behavior and degree of ordering of AuNP films through changes in surface pressure, with the resulting structures also influenced by particle size and ligand length [53]. Evaporation can continuously supply particles to the air–water interface [54]. Using this approach, Guo et al. organized polyvinylpyrrolidone (PVP)-modified AuNPs at the interface into a hexagonally close-packed monolayer with interparticle gaps below 2 nm and transferred the assembled film onto different solid supports [55].

To enable flexible integration, polymer supports can be incorporated during interfacial assembly or film transfer. Tian and Zhang co-assembled Au octahedra with a styrene–ethylene–butylene–styrene (SEBS) block copolymer at an air–liquid interface, partially embedding the particles in the polymer to form a free-standing superlattice that could be transferred onto PDMS (Figure 2B) [56]. In another study, a Langmuir–Blodgett-assembled Ag nanocube superlattice film was transferred onto an ultrathin poly(methyl methacrylate) (PMMA) layer. A guard ring in the device reduced the strain experienced by the active region, allowing the SERS response to remain stable after repeated stretching (Figure 2C) [13]. The same platform further combined the interfacially assembled SERS film with active sweat extraction for on-body drug monitoring.

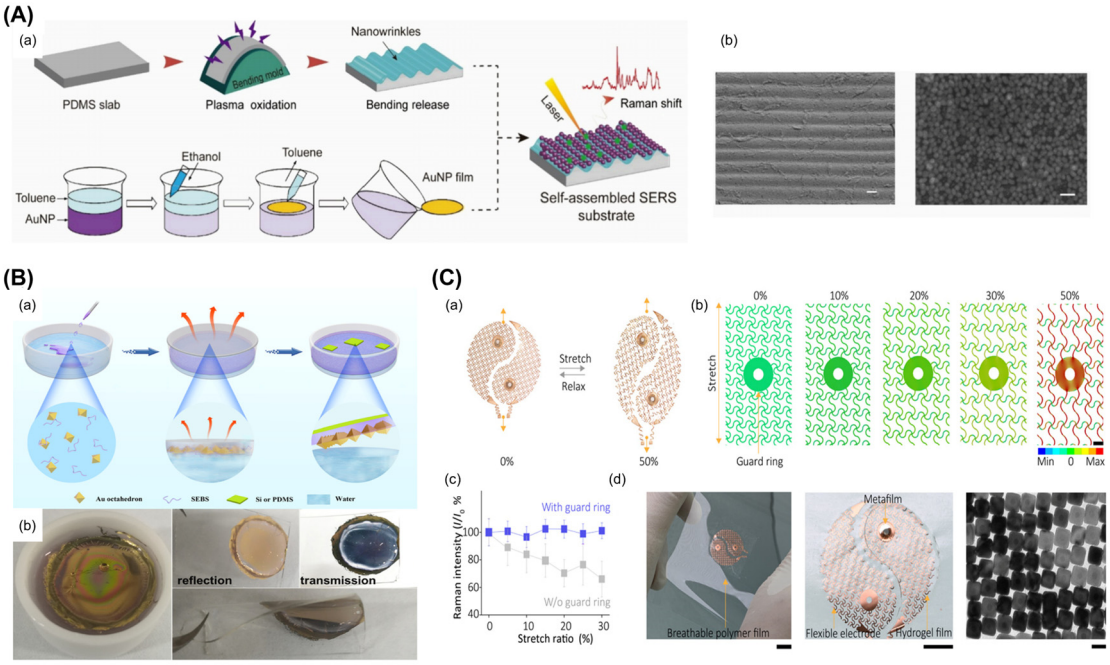


Figure 2. Representative fluid-interface self-assembly strategies for flexible and wearable SERS substrates. (**A**) Liquid–liquid interfacial assembly of AuNP films and their transfer onto nanowrinkled PDMS: (**a**) schematic of substrate preparation and AuNP-film transfer; (**b**) SEM images of the assembled AuNP structures, with scale bars of 1 μm (left) and 100 nm (right). Adapted with permission from Ref. [50]. Copyright 2024 American Chemical Society; permission conveyed through Copyright Clearance Center, Inc. (**B**) Air–water interfacial co-assembly of Au octahedra and SEBS into a free-standing superlattice transferable to PDMS: (**a**) schematic illustration of the interfacial co-assembly and transfer process; (**b**) photographs of the resulting flexible superlattice film under reflection and transmission and during bending. Reproduced with permission from Ref. [56]. Copyright 2023 Royal Society of Chemistry; permission conveyed through Copyright Clearance Center, Inc. (**C**) Langmuir–Blodgett (LB)-assembled Ag nanocube superlattice integrated into a strain-isolated flexible SERS platform: (**a**) schematic of the device before and after stretching, (**b**) simulated strain distribution around the guard ring under different applied strains, (**c**) SERS intensity under stretching with and without the guard ring, and (**d**) optical and microscopy images of the integrated wearable device and Ag nanocube metafilm. Reproduced from Ref. [13] with permission from AAAS.

2.2. Evaporation-Induced Self-Assembly

Evaporation-induced self-assembly relies on particle transport during droplet drying, allowing nanoparticles to be deposited and fixed directly on the final support [41]. The resulting deposition morphology is influenced mainly by the evaporation geometry and contact-line motion. When the three-phase contact line is pinned, capillary replenishment transports particles toward the droplet edge, producing ring-shaped deposits. Under confined conditions, meniscus motion or stick–slip motion can further generate stripes or annular bands, while capillary flow can also carry particles to the end faces or inner walls of microstructures. Because deposition occurs directly on the final support, this route avoids separate film formation and transfer. The deposition location varies with substrate wettability and evaporation conditions.

On planar supports, contact-line behavior determines whether particles undergo localized enrichment or controlled organization. When the contact line remains pinned, the higher evaporation flux near the droplet edge drives capillary replenishment, concentrating both particles and analytes at the three-phase contact line. Rourke-Funderburg et al. used wax printing and thermal treatment to restrict liquid penetration into nitrocellulose paper, producing AuNP coffee-ring deposits whose morphology varied with particle

concentration (Figure 3A) [57]. The resulting platform was subsequently used for SERS detection of 4-mercaptobenzoic acid (4-MBA) and bacterial samples. Further confinement of the droplet geometry can improve the positional consistency of deposition. Farcau et al. confined Au colloidal droplets between a vertical glass slide and a horizontal substrate and generated parallel AuNP stripes through periodic pinning and depinning of the contact line. The p-aminothiophenol (pATP) signal varied by approximately ±13% across different positions in the central region of the stripes, substantially less than the approximately ±90% variation observed from the ring edge to the center of conventionally drop-cast samples (Figure 3B) [58]. Pinned deposition is therefore suited to simultaneous enrichment within a defined region, whereas confined stick–slip motion is more favorable for generating periodic structures at controlled positions.

Meniscus-mediated assembly under localized heating can enrich particles at optical-fiber end faces, while stick–slip motion during fiber withdrawal can generate periodic annular bands along tapered sidewalls [59,60]. Kang et al. used evaporation-driven convective self-assembly to deposit AuNPs onto the end face of a flexible silk fibroin optical fiber, creating a fiber-optic SERS probe (Figure 3C) [61]. For elastic supports, deformation can densify particle assemblies or alter preformed hotspots. Wrinkles formed upon release of prestrained PDMS can compact particles in coffee-ring regions [62], whereas the SERS intensity of preassembled AuNP aggregates decreases during biaxial stretching as interparticle coupling weakens [63].

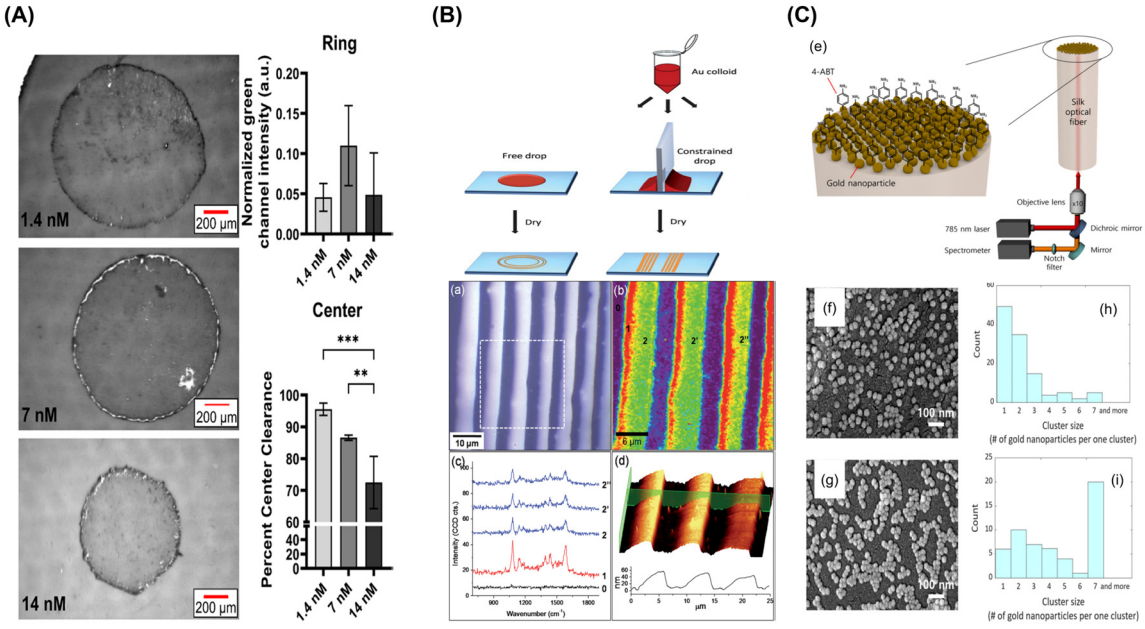


Figure 3. Representative evaporation- and meniscus-induced assembly of SERS-active nanoparticles. (**A**) AuNP coffee rings formed at concentrations of 1.4, 7, and 14 nM, with corresponding analysis of ring intensity and center clearance. Adapted from Ref. [57], licensed under CC BY 4.0. (**B**) Periodic AuNP stripes formed by confined-meniscus stick–slip assembly, with free-drop drying shown for comparison: (**a**) optical image of the periodic stripe pattern, (**b**) corresponding spatial mapping, (**c**) representative Raman spectra collected at selected positions, and (**d**) surface topography and height profile of the stripe structure. Reproduced with permission from Ref. [58]. Copyright 2013 Royal Society of Chemistry; permission conveyed through Copyright Clearance Center, Inc. (**C**) AuNP-decorated silk fiber-optic SERS probe prepared by evaporation-driven convective self-assembly: (**e**) schematic of the AuNP-functionalized silk optical fiber and Raman measurement configuration, (**f**,**g**) representative SEM images of the AuNP assemblies, and (**h**,**i**) corresponding distributions of AuNP cluster size. Adapted from Ref. [61], licensed under CC BY 4.0.

2.3. Template-Assisted Self-Assembly

Template-assisted self-assembly uses predefined micro- or nanostructures to confine particle deposition to selected locations. The geometry and periodicity of the template can further regulate the position and size of particle clusters as well as intracluster spacing [64,65]. Such templates may consist of micro/nanopatterns or colloidal crystals, while particles are directed into confined regions through capillary action, electrophoresis, or electrohydrodynamic transport. When electrophoretic or electrohydrodynamic driving is combined with a template, the external field influences particle transport and local orientation, whereas the overall particle distribution remains constrained by the template geometry [38]. For flexible SERS interfaces, the template defines the initial particle distribution, while subsequent transfer, fixation, and deformation of the support affect structural retention and the resulting spectral response.

Template periodicity can alter diffractive coupling between particle clusters, thereby tuning the lattice resonances and optical response of the array. Matricardi et al. used a patterned PDMS mold to confine Au nanospheres within periodic cavities and assemble them into particle-cluster arrays. When the array resonance approached the 785 nm excitation wavelength, the SERS response was markedly enhanced [66].

Templates also guide the fabrication of particle arrays and their subsequent integration with supports. Garg et al. assembled AuNP microspot arrays within microporous templates by capillary action and embedded them into a polyurethane layer through UV micro/nanoimprinting, followed by transfer onto polyethylene terephthalate (PET), semipermeable membranes, and elastic textiles [67]. Particle capture within templates can also be accelerated by controlling evaporation. Laghrissi et al. developed a rapid template-assisted self-assembly method in which AgNPs were directly captured in patterned PDMS traps to form dense particle assemblies. The resulting substrate was used for SERS detection of 2-naphthalenethiol, with an enhancement factor of approximately 10^4 obtained for assemblies of 50 nm AgNPs (Figure 4A) [68].

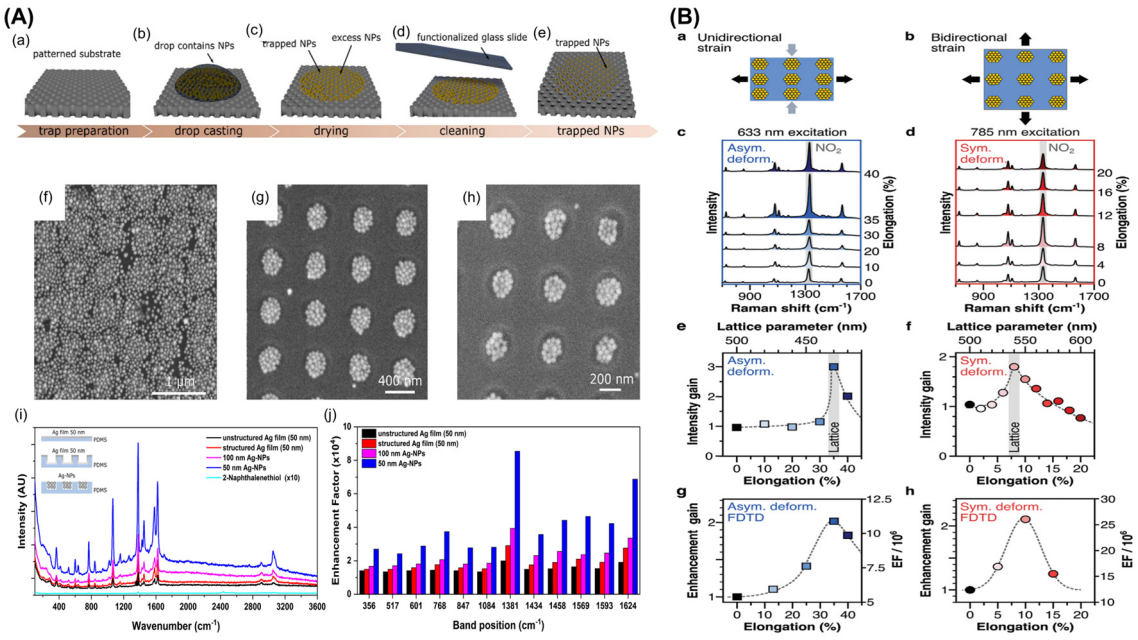


Figure 4. Representative template-assisted self-assembly strategies for plasmonic nanoparticle structures. (**A**) Rapid template-assisted self-assembly of AgNPs in patterned PDMS: (**a**–**e**) schematic

sequence of trap preparation, drop casting, drying, cleaning, and particle trapping; (**f**–**h**) representative SEM images of the assembled AgNP structures; (**i**) representative SERS spectra; and (**j**) enhancement factors at selected Raman bands. Adapted from Ref. [68], licensed under CC BY 4.0. (**B**) Mechanically tunable AuNP superlattices on flexible PDMS: (**a**,**b**) schematics of unidirectional and bidirectional strain; (**c**,**d**) Raman spectra under asymmetric and symmetric deformation at different elongations; (**e**,**f**) corresponding intensity gains; and (**g**,**h**) finite-difference time-domain (FDTD)-calculated enhancement factors. Reprinted with permission from Ref. [69]. Copyright 2021 Wiley-VCH GmbH.

After transfer to a flexible support, deformation itself can become a tuning parameter. Charconnet et al. transferred AuNP superlattices onto PDMS, such that stretching primarily changed the intercluster lattice period while leaving the interparticle gaps within the clusters largely unchanged (Figure 4B). As the lattice resonance approached the excitation wavelength, the SERS signal increased to approximately three times its initial value [69].

Template-defined structures can be combined with interfacial assembly. Li et al. used polystyrene (PS) sphere templates to fabricate a PDMS inverse-opal structure and then transferred an AuNP film assembled at an oil–water interface onto the metallized nanobowl surface. The periodic cavities and interparticle gaps between AuNPs jointly contributed to electromagnetic enhancement, and the resulting substrate was used for uric acid quantification in collected tear samples [70].

Table 1 summarizes the three self-assembly routes in terms of hotspot formation, structural control, flexible integration, and fabrication characteristics.

Table 1. Comparison of three self-assembly strategies for wearable SERS substrates.

Self-Assembly Strategy	Hotspot Formation	Structural Control	Flexible Integration	Fabrication Characteristics and Limitations
Fluid-interface self-assembly	Interfacial preassembly into a film followed by whole-film transfer	Interparticle spacing; film density, continuity, and area	Whole-film transfer; stability affected by film-support adhesion	Dense film formation over large areas; risk of transfer-induced defects [13,50,56]
Evaporation-induced self-assembly	Direct deposition at the liquid-solid interface or contact line	Deposition location; local enrichment, annular bands, and stripes	Direct assembly on paper-based, porous, or final supports	Short processing route; sensitive to evaporation, wettability, and contact-line motion [57–63,71]
Template-assisted self-assembly	Template-confined assembly followed by fixation or transfer	Particle-cluster position and size; array periodicity and hierarchical morphology	Embedding, imprinting, or transfer; deformation-mediated tuning of periodicity and coupling	Well-defined geometric control; more processing steps with potential error accumulation [66–70]

2.4. Integration of Self-Assembled SERS Interfaces with Wearable Sampling and Optical Readout

After self-assembly, plasmonic structures are fixed within the components that contact or receive the biofluid. In skin-mounted sweat platforms, the SERS-active region can be integrated with microfluidic channels, absorbent paper, or sweat-extraction modules that transport sweat to the sensing area [13,72]. Flexible polymer films, paper substrates, and hydrogel-supported structures have all been used to hold the assembled plasmonic layer within the wearable device. In microneedle systems, the plasmonic coating is formed

directly on the needle surface, where it contacts the sampled region during insertion [73,74]. These device structures affect both sample delivery to the SERS-active region and access of the Raman excitation and collection optics.

Raman excitation and spectral acquisition are still performed with an external optical instrument in the wearable systems discussed here. Wang et al. integrated a Langmuir–Blodgett-assembled Ag nanocube metafilm with an iontophoresis-assisted sweat-extraction system and acquired SERS signals from the back side of the film while the device was attached to the skin [13]. Sung et al. integrated a soft microfluidic SERS patch with external Raman readout and separately evaluated an ex situ portable Raman configuration. They examined the effects of probe position, device curvature, and the interval between sweat filling and spectral acquisition. In their benchtop and human trials, SERS measurements were typically performed within ~15 min after sweat filling was completed [75]. These examples follow the general measurement chain illustrated in Figure 1D, in which the wearable SERS interface remains optically coupled to an external Raman readout unit.

For microneedle SERS, the active surface may remain embedded in a skin model during measurement. Park et al. deposited Langmuir–Blodgett-assembled GNR@Ag layers onto transparent NOA65 microneedles. Backside excitation and signal collection were demonstrated while the microneedles remained inserted in an agarose skin phantom, so the spectra could be acquired without withdrawing the microneedles from the model [73]. The transparent NOA65 body provided an optical path to the coated microneedle surface, enabling backside excitation and signal collection while the microneedles remained inserted.

The Raman readout unit remains a separate component in these wearable SERS systems. Wang et al. identified the size of the Raman readout system as a limitation and demonstrated a proof-of-concept miniaturized Raman system for portable measurement [13]. Sung et al. further showed that probe alignment and focusing conditions can change measurement consistency when a portable Raman instrument is used [75]. For online monitoring, sample collection and spectral acquisition also need to be distinguished. On-body sampling refers to collection while the device is worn. In situ spectral readout requires Raman acquisition without removing the sensing interface. Time-resolved or continuous monitoring additionally requires repeated spectral acquisition together with sufficient renewal of the sample at the active region.

3. Biofluid Sensing Applications and Progress Toward Online Readout

When self-assembled SERS substrates are used for biofluid analysis, the sampling and interfacial constraints differ among biofluids. Sweat is affected by secretion rate, evaporation, and mixing between newly secreted and residual sweat, whereas interstitial fluid is limited by the stratum corneum barrier and low sampling throughput [76,77]. Tear samples are limited in volume and subject to competitive protein adsorption, while wound exudate presents a high protein load and a complex matrix [78,79]. This section is organized around these four biofluids and focuses on studies in which the assembled structures directly constitute the SERS-active interface.

3.1. Sweat Sensing Applications

Sweat can be collected directly from the skin surface and is continuously produced during exercise, thermal stimulation, or pharmacological stimulation, making it one of the most extensively studied biofluids in wearable biochemical monitoring [80–84]. Lactate and pH can reflect exercise-related metabolism and changes in the acid–base status of sweat [85]. Uric acid, creatinine, and glucose have also been explored for monitoring metabolic changes and for the assessment of renal function or glucose metabolism [80–84,86], whereas cortisol and drug molecules are used to track stress-related changes and drug exposure, respec-

tively [13,83,87]. However, sweat volume and flow rate vary with the individual, body site, and exercise conditions [88]. Limited sample volume and mixing between newly secreted and residual sweat can further change both the amount of sample reaching the sensing region and the time point represented by that sample [72,81,82,89–91]. Related studies have therefore focused mainly on three aspects: the construction of ordered interfaces, the stability of quantitative measurements, and sweat collection.

Ordered self-assembled structures can provide flexible SERS interfaces with relatively uniform responses and support different analytical modes [92,93]. Hu et al. developed an Au@Ag/silk fibroin (SF) inverse-opal interface and a binary nanosphere array, both integrated with PDMS microfluidic channels. The former was used for label-free analysis of creatinine and uric acid in sweat from healthy volunteers, whereas the latter incorporated a cortisol aptamer for the detection of cortisol and pH during exercise-induced sweating. In these two studies, the periodic flexible interfaces supported molecular-fingerprint-based multianalyte detection and could also be adapted to additional targets by incorporating specific recognition elements.

Under on-body conditions, measurement-site variability can affect quantitative results, while sustained deformation may compromise structural stability [94]. Sung et al. incorporated enzymatic signal conversion and rhodamine 6G (R6G) internal-standard normalization into a gold nanorod (AuNR)/filter-paper SERS reaction zone. They quantified creatinine and glucose in sweat samples from 13 participants and cross-validated the results using colorimetric measurements (Figure 5A) [75]. A separate challenge arises from deformation during wear. In another study, the AuNP superlattice was patterned into discrete micron-scale domains to redistribute stress and suppress cracking. The substrate maintained a relatively stable SERS response after 40 h of on-body wear and was used to monitor sweat pH, lactate, and sweat volume [95].

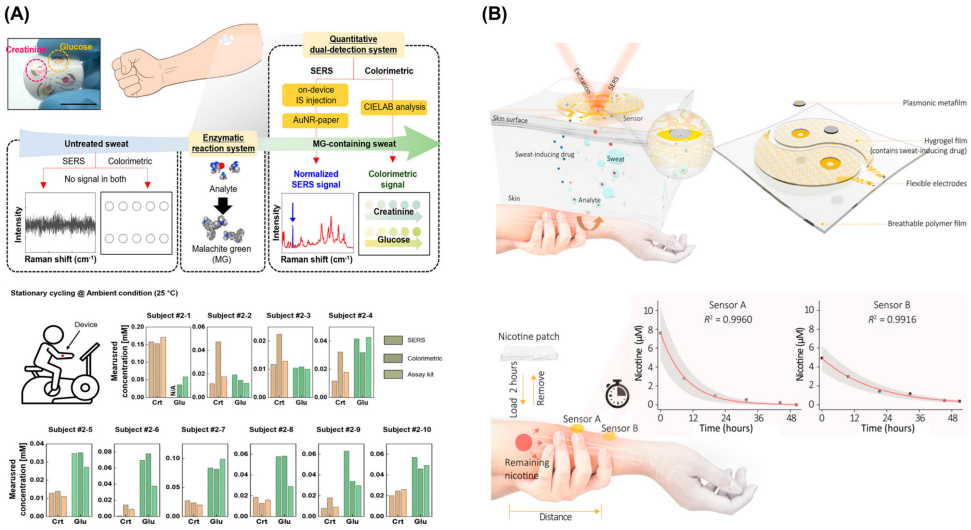


Figure 5. Representative self-assembled SERS strategies for wearable sweat monitoring. (**A**) Skin-mounted soft microfluidic SERS platform for quantitative sweat analysis, showing R6G internal-standard normalization and colorimetric cross-validation for creatinine and glucose. Reproduced from Ref. [75] with permission from Springer Nature. (**B**) Wearable plasmonic–electronic sensor integrating iontophoresis-assisted sweat extraction with an ordered Ag nanocube superlattice film for on-body nicotine monitoring. Reproduced from Ref. [13] with permission from AAAS.

The platforms described above rely on exercise or external heating to induce sweating, while the patches themselves mainly serve to collect and analyze sweat. On-demand measurements under low-sweat conditions require the device to actively induce sweat secretion. Wang et al. integrated a flexible SERS interface with an acetylcholine iontophore-

sis module, enabling localized sweat induction and time-resolved monitoring of nicotine levels (Figure 5B) [13]. This design allowed sweat to be obtained on demand even under low-sweat conditions and supported spectral acquisition at predefined time points.

The focus of sweat SERS research has gradually expanded beyond performance enhancement to include quantification error, deformation during wear, and active sampling [13,75,94–96]. Long-term biochemical changes are still mainly tracked through intermittent spectral acquisition.

3.2. Interstitial Fluid Sensing Applications

Unlike sweat, which can be collected from the skin surface, ISF is distributed within the extracellular spaces of skin tissue and is in continuous exchange with the local microcirculation. Representative ISF targets include uric acid and other metabolites, local pH, and exogenous drugs [73,74,97]. These measurements can provide information on metabolic status, the local acid–base environment, and drug transport, respectively [73,74,98,99]. Because ISF sensing requires access across the stratum corneum and only limited sample volumes are available, microneedles have become important platforms for ISF sampling and on-needle SERS analysis [99–104]. For self-assembled SERS microneedles, the microneedle interface must provide a high density of hotspots. It also needs to facilitate the transport of small amounts of ISF to the active region and maintain particle-layer stability during insertion. A representative microneedle-based SERS sensing workflow is illustrated in Figure 6.

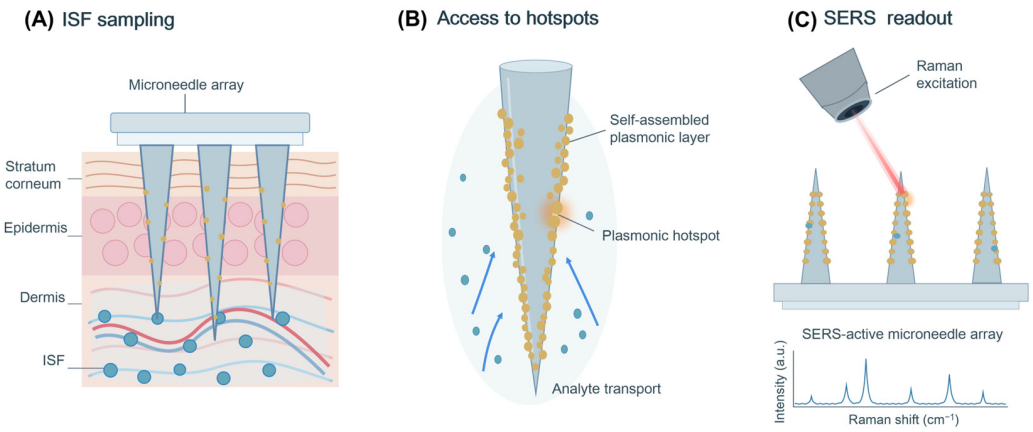


Figure 6. Conceptual schematic of microneedle-based SERS sensing of interstitial fluid. (**A**) ISF access by microneedle penetration. (**B**) Transport of analytes to self-assembled plasmonic hotspots. (**C**) Raman readout from the SERS-active microneedle array.

In most self-assembled SERS microneedles, the particle layer is fixed on the needle before insertion, allowing ISF sampling and SERS detection on the same needle. For on-needle detection, the small amount of ISF must first reach the hotspots. Liu et al. fabricated AuNP/PMMA microneedles through liquid–liquid interfacial assembly. The hydrophilic surface promoted the transport of simulated ISF along the microneedles to the active region, enabling uric acid and pH analysis in an agarose model [74]. When spectra are acquired directly with the microneedles remaining inserted, the main constraints shift to the optical path and particle-layer adhesion during insertion. Park et al. repeatedly transferred interfacially assembled Ag-coated gold nanorod (GNR@Ag) monolayers onto transparent NOA65 microneedles to form a multilayer SERS coating. The coating remained attached during insertion and withdrawal, and backside spectra were acquired with the microneedles remaining inserted in an agarose skin model. The pH response was further validated in ex vivo porcine skin [73]. The former focuses on sample transport to the active

region, whereas the latter addresses optical readout in the inserted state. In SERS-based pH sensing, pH is not measured from the Raman signal of hydrogen ions themselves. Surface-bound pH-responsive Raman reporters such as 4-mercaptobenzoic acid (4-MBA) undergo protonation/deprotonation, leading to changes in characteristic vibrational bands that can be quantified from peak positions or intensity ratios [73,74]. Potentiometric sensors offer a simpler approach when pH is the sole target. SERS, however, enables pH and molecular analytes to be measured on the same plasmonic interface, which is useful for multiparameter SERS sensing and for interpreting pH-dependent biochemical signals.

Another strategy is to form SERS hotspots after ISF sampling. Li et al. used hyaluronic acid (HA)/methacrylated hyaluronic acid (HAMA) microneedles to collect ISF containing hemoporfin (Hp). After the microneedles were withdrawn, Au/Ag nanocages aggregated through ion bridging were sprayed onto the sample-loaded needles to generate SERS hotspots [98]. In mouse experiments, characteristic Hp peaks appeared approximately 21 min after administration and gradually increased thereafter, enabling time-course tracking of in vivo drug transport.

Preassembled microneedles can bring ISF into contact with the SERS-active interface and enable spectral readout on the same needle, whereas strategies that construct hotspots after sampling have been used for drug tracking in mouse ISF but do not support direct spectral acquisition with the microneedles left in place. Platforms that preimmobilize SERS hotspots and allow repeated spectral acquisition while remaining inserted after in vivo contact with ISF are still uncommon.

3.3. Tear Sensing Applications

Tears can be collected noninvasively and contain components such as proteins, metabolites, and electrolytes. Changes in these components have been explored as indicators of ocular surface status and systemic metabolic and inflammatory changes [105–108]. However, tear samples are limited in volume, and competitive protein adsorption can occupy SERS-active sites, while salts and other endogenous components may increase background interference [106,107,109]. These factors can affect target access to hotspots and the consistency of SERS signals across different measurement sites.

For biomarkers detectable from intrinsic Raman signatures, periodic hotspots can reduce signal variability across measurement sites. Li et al. integrated an interfacially assembled AuNP film with a PDMS inverse-opal structure, achieving an RSD below 5% for uric acid quantification in tears from patients with hyperuricemia [70]. Cui et al. used an interfacially assembled AuNP film on MXene paper to convert glucose concentration into a Raman signal through an enzymatic reaction and examined the correlation between tear glucose concentration and blood glucose levels [110]. Complex tear matrices can also occupy SERS-active surfaces. Zhao et al. incorporated matrix separation into a SiO_2@Au@AuNPs binary nanosphere array [106]. The upper AuNP/Au layer provided hotspots, while periodic pores directed some nontarget components to a lower inactive region, reducing interference near the hotspots. Integrated into a tear-testing cartridge, the structure was used for bilirubin analysis and identification of tear samples from patients with jaundice (Figure 7).

Beyond quantification of individual biomarkers, overall tear spectral profiles have also been used for sample classification, making signal consistency across measurement sites particularly important. Kim et al. formed a self-assembled hexagonally close-packed PS nanosphere monolayer and subsequently deposited Au to construct an Au/HCP-PS array [107]. Combined with portable Raman spectroscopy and multivariate analysis, the platform enabled preliminary discrimination between patients with breast cancer and healthy controls in a small clinical tear cohort.

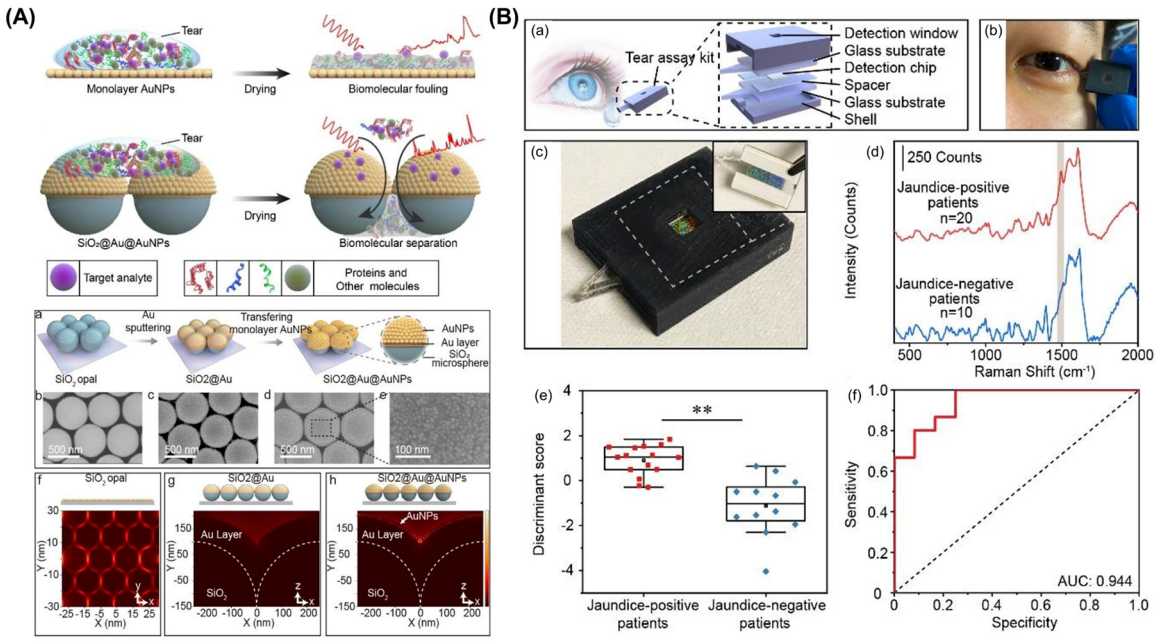


Figure 7. Representative self-assembled SERS interface for tear analysis. (**A**) SiO_2@Au@AuNPs binary nanosphere array for biomolecular separation and SERS sensing in tears, showing the anti-fouling/separation mechanism and substrate construction: (**a**) preparation of the SiO_2@Au@AuNPs structure; (**b**–**d**) SEM images of SiO_2 opal, SiO_2@Au, and SiO_2@Au@AuNPs structures, respectively; (**e**) high-magnification SEM image of the SiO_2@Au@AuNPs structure; and (**f**–**h**) calculated electromagnetic-field distributions of the corresponding structures. (**B**) Clinical tear-assay platform for jaundice diagnosis: (**a**) schematic of the tear assay kit; (**b**) tear collection from the eye; (**c**) photograph of the tear assay kit; (**d**) representative Raman spectra of jaundice-positive and jaundice-negative patients; (**e**) discriminant-score analysis; and (**f**) receiver operating characteristic (ROC) curve for jaundice classification. ** indicates $p < 0.01$. Reproduced from Ref. [106] with permission. Copyright© Wiley-VCH GmbH.

Current tear-sensing studies have addressed flexible-substrate integration, matrix separation, and control of measurement-site variability. Continuous sampling and continuous spectral acquisition during on-eye wear have not yet been demonstrated.

3.4. Wound Exudate and Wound-Related Sensing Applications

Wound exudate contains proteins, metabolites, and inflammation-related molecules and may also carry infectious pathogens [111–113]. Detection and changes in the abundance of bacteria such as *Pseudomonas aeruginosa*, *Staphylococcus aureus*, and *Escherichia coli* can help identify infecting pathogens and track bacterial burden [112,113], while characteristic metabolites such as pyocyanin can reflect the metabolic activity of *P. aeruginosa* [114,115]. However, high protein loads and mixed blood and tissue debris can cause nonspecific adsorption, spectral interference, and blockage of SERS hotspots [116]. These complex components can hinder target access to hotspots and further complicate flexible wound sampling and selective capture [117].

Nguyen et al. used template-confined assembly to form AuNP oligomers and stabilized their subnanometer interparticle gaps by crosslinking, creating a stable SERS-enhancing interface for longitudinal monitoring of pyocyanin in biofilm effluent [115]. Direct pathogen identification typically begins with bacterial capture from the wound surface. Guo et al. assembled and encapsulated Au nanostars on graphene to fabricate a flexible SERS tape conformable to wound surfaces [113]. After incorporation of a photoresponsive capture molecule, the tape could capture and release bacteria from burn wounds in mice, followed by SERS identification after 8 h of culture. In contrast to this

capture–release–culture approach, Zhou et al. transferred an interfacially assembled AuNP film onto PDMS and used an antibody sandwich assay to achieve culture-free identification directly on the flexible interface [112]. The platform was used for time-course detection in infected wounds in mice and was further validated for bacterial identification in clinical wound tissue samples. A conceptual overview of wound-related SERS sensing is provided in Figure 8.

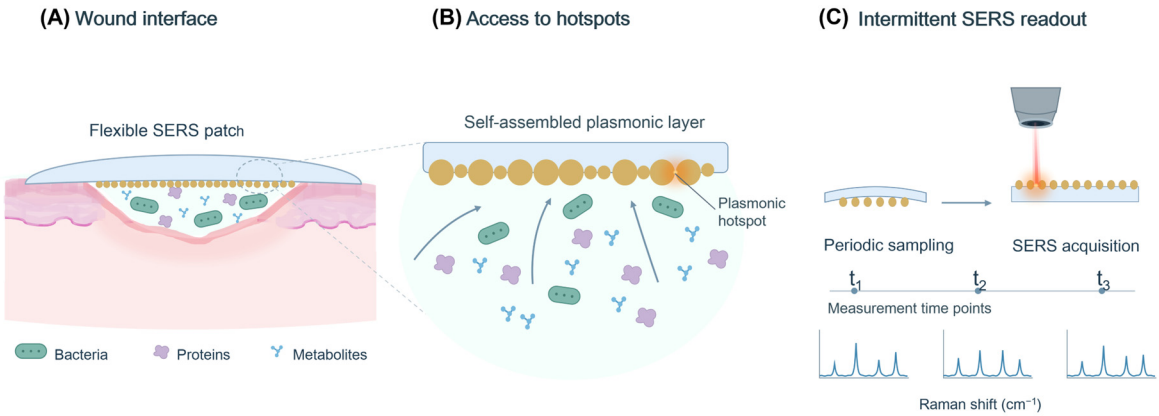


Figure 8. Conceptual schematic of self-assembled SERS interfaces for wound-related sensing. (**A**) Contact of a flexible SERS interface with wound exudate. (**B**) Access of wound-related targets to self-assembled plasmonic hotspots. (**C**) Intermittent SERS readout at representative measurement time points.

Table 2 summarizes representative studies in which self-assembled structures directly constitute the SERS-active interface and are integrated with biofluid-sampling or sensing platforms. The selected studies illustrate typical applications across different biofluids.

Most studies listed in Table 2 rely on transfer of preassembled films formed at fluid interfaces or combine interfacial assembly with template confinement before integration with supports such as paper, PDMS, silk fibroin films, or microneedles. Evaporation-induced assembly currently appears mainly in combined routes, with relatively few studies using it alone for wearable biofluid analysis. Among the biofluids considered, sweat sensing has undergone more extensive validation under on-body conditions and with dynamic spectral readout, whereas studies involving ISF, tears, and wounds still rely more heavily on model or ex vivo tissue experiments, post-collection analysis, and animal or clinical sample validation, respectively. The quantitative metrics summarized in Table 2 also show substantial heterogeneity in performance reporting. Some studies provide target-specific limits of detection and calibration ranges, while others emphasize substrate reproducibility, mechanical stability, or time-resolved operation. More consistent reporting of analytical range, LOD, acquisition time, and inter-device or inter-batch reproducibility would facilitate comparison across wearable SERS platforms.

Current self-assembled wearable SERS platforms remain dominated by small-molecule metabolites and physicochemical parameters, including glucose, uric acid, lactate, and pH. Detection of disease-related biomarkers often relies on additional molecular-recognition or signal-conversion mechanisms. Aptamer-mediated recognition has enabled cortisol sensing in sweat [93], while antibody-based sandwich assays have supported selective culture-free detection of wound pathogens [112]. Bilirubin-based jaundice classification in tears has also extended SERS analysis beyond direct metabolite quantification [106]. The analytical scope of wearable SERS is therefore beginning to move toward more clinically relevant targets.

Table 2. Representative self-assembled SERS interfaces for wearable biofluid sensing: reported analytical metrics and validation.

Biofluid	Assembly Route and Integrated Structure	Target(s)	Reported Analytical Metrics	Validation and Readout	Author (Ref.)
Sweat	Template-assisted + fluid-interface: SF-supported PS opal/Au/Ag binary nanosphere array–microfluidic patch	Cortisol, pH	Range: cortisol 0.1–1000 nM; pH 4–7 RSD: 7.2% Substrate-level LOD (R6G): 33 pM	On-body sweat sampling; post-collection spectral acquisition	Hu et al. [93]
Sweat	Fluid-interface: AuNR monolayer/filter paper–PDMS microfluidic reactor	Creatinine, glucose	Range: glucose 0.01–0.8 mM Benchtop calibration fit: creatinine R^2 = 0.907; glucose R^2 = 0.89 Readout timing: typically within ~15 min after reservoir filling	On-body sweat sampling; post-collection spectral acquisition; portable Raman configuration evaluated ex situ	Sung et al. [75]
Sweat	Template-assisted + evaporation-induced: patterned AuNP superlattice–PDMS microfluidic patch	pH, lactate, sweat volume	Range: pH 5.0–7.0; lactate 5–20 mM Wear stability: stable SERS response over 40 h	On-body wear; continuous pH monitoring; lactate measurement during exercise	Ye et al. [95]
Sweat	Fluid-interface: LB-assembled Ag nanocube film–iontophoresis-assisted sweat patch	Nicotine and other exogenous molecules, pH	LOD: 100 nM (nicotine) Range: 0.1–10 μM Acquisition time: 1 s	Iontophoresis-assisted on-body sweat sampling; time-resolved spectral acquisition	Wang et al. [13]
ISF	Fluid-interface: AuNP layer–PMMA microneedles	Uric acid, pH	Range: uric acid 40–640 μM; pH 4.5–6.5 RSD: 4.4–6.7%	Agarose skin model; spectral acquisition after insertion	Liu et al. [74]
ISF	Fluid-interface: GNR@Ag layer–transparent NOA65 microneedles	pH	Range: pH 4–8 Repeatability: 6 pH cycles Substrate-level LOD (R6G): 10^{-10} M	Agarose skin phantom; backside readout while inserted; ex vivo porcine skin validation after insertion–withdrawal	Park et al. [73]
Tears	Template-assisted + fluid-interface: AuNP/PDMS inverse-opal substrate	Uric acid	LOD: 6.03 μM (artificial tears) Range: 25–150 μM RSD: <5% EF: 4.22×10^4 Analysis time: $\leq$5 min	Clinical tear samples; post-collection quantification	Li et al. [70]

Table 2. *Cont.*

Biofluid	Assembly Route and Integrated Structure	Target(s)	Reported Analytical Metrics	Validation and Readout	Author (Ref.)
Tears	Fluid-interface: AuNP/MXene paper-based sensing strip	Glucose	LOD: 0.39 μM Range: 1–50 μM RSD: 11.7% EF: 3.7×10^5	Clinical tear samples; post-collection analysis	Cui et al. [110]
Tears	Template-assisted + fluid-interface: SiO_2@Au@AuNPs binary nanosphere array–assay component	Bilirubin, jaundice classification	LOD: 10^{-9} M (free bilirubin in PBS) RSD: 7.9% Clinical classification: AUC = 0.944	Clinical tear samples; post-collection classification	Zhao et al. [106]
Wound	Fluid-interface: AuNP/PDMS capture substrate + Au@Ag probes	*E. coli*, *S. aureus*, *P. aeruginosa*	LOD: 2.79/3.42/4.52 CFU mL^{-1} for *E. coli*/*S. aureus*/*P. aeruginosa* Range: ~10^0–10^7 CFU mL^{-1} Acquisition time: 1 s	Infected mouse wounds; time-course detection; clinical wound tissue; post-collection validation	Zhou et al. [112]

Note: "+" indicates combined self-assembly routes. LOD, limit of detection; EF, enhancement factor; RSD, relative standard deviation; AUC, area under the ROC curve. Only values explicitly reported in the original studies are included. LODs obtained using Raman model probes are identified as substrate-level metrics. "On-body sampling" denotes biofluid collection while the device is worn. "In situ readout" denotes spectral acquisition while the sensing interface remains in place or inserted. "Time-resolved readout" denotes repeated measurements at predefined time points, while "continuous monitoring" is used only when a continuous or real-time measurement series was explicitly reported.

4. Conclusions and Outlook

This review classifies self-assembly strategies for wearable SERS into three categories—fluid-interface, evaporation-induced, and template-assisted self-assembly—according to the dominant process governing particle organization. The classification emphasizes how hotspots are formed and how the assembled structures relate to the final support, while combined routes are also used in practical devices. Self-assembled hotspots have now been applied to the analysis of multiple biofluids. In sweat sensing, quantitative measurements under on-body conditions have been demonstrated [75], and some platforms have enabled continuous or time-course spectral acquisition [13,95], placing sweat closest to online readout among the biofluids considered here. Studies involving interstitial fluid, tears, and wounds, by contrast, still rely more heavily on models, ex vivo tissues, or post-collection analysis [70,73,74,106,110,112].

Many studies currently evaluate substrate reproducibility using the RSD from a limited number of measurement sites, making it difficult to assess variations across the entire sensing area and between batches. Fabrication defects can introduce spatial nonuniformity in SERS-active regions, while deformation during wear may further alter interparticle spacing or particle attachment. Guard rings and discrete superlattice domains have shown the ability to mitigate deformation-induced effects [13,95]. However, few studies systematically report the actual area over which stable SERS responses are maintained or how these regions change spatially before and after wear. Large-area Raman mapping combined with structural characterization could directly reveal changes in hotspot distribution associated with wear.

Long-term wearable use also raises material-safety considerations that are not captured by SERS performance alone. Gold is generally favored for its chemical stability, although the biological response to Au nanostructures still depends on particle size, surface chemistry, and exposure conditions [118,119]. Silver nanostructures can undergo dissolution and release Ag ions in biological environments, making exposure conditions particularly relevant for prolonged skin contact, microneedle insertion, and direct wound contact [120,121]. Nanoparticle detachment during bending, abrasion, or insertion may further affect both sensing performance and local exposure. Stable immobilization, encapsulation, and protective coatings can limit direct particle contact or release while preserving access of analytes to the SERS-active region. Long-term wearable SERS evaluation therefore needs to consider particle retention, ion release, and local cytocompatibility together with analytical stability.

When applied to real biofluids, protein adsorption can hinder target access to hotspots, while probe repositioning can change the effective sampling area [14,18,106,109]. Internal-standard correction and assembled structures with matrix-separation capabilities have been used in sweat and tear sensing to improve quantitative stability in complex matrices [75,106]. Spike-recovery measurements can reveal matrix-induced quantitative bias. Method comparison using the same biofluid sample provides a more direct test of SERS quantification, whereas comparison with blood measurements mainly reflects physiological correlations between different biofluids. During continuous or time-course spectral acquisition, inadequate replacement of the previous sample can also make it difficult to attribute spectral changes directly to physiological processes.

Further expansion toward complex biomarkers depends on recognition strategies that remain selective and stable in real biofluids. Molecularly imprinted interfaces provide an alternative to biological recognition elements for selected targets [122]. Multivariate analysis and machine-learning-assisted classification can also support the interpretation of multianalyte measurements or highly overlapping spectral patterns [79,107,123]. Clinical validation with real samples and independently tested datasets becomes more important as the analytical targets and spectral information grow more complex. Self-assembled hotspots have already been integrated with a range of wearable biofluid-sensing interfaces, but substantial differences remain in how close individual applications are to online monitoring. Sweat sensing has a relatively strong foundation in on-body testing and repeated spectral acquisition; future studies should expand sample sizes and strengthen independent method validation under matched conditions. Studies involving interstitial fluid, tears, and wounds still lack sufficient evidence from in situ measurements in humans or during long-term attachment. Biofluids beyond those emphasized in this review involve different sampling requirements. Readily accessible fluids can be collected more directly for wearable or point-of-care sensing, while blood-derived samples generally require invasive collection and are more commonly analyzed ex vivo. In addition, the stability of large-area SERS-active regions before and after wear remains poorly characterized. Addressing these validation gaps will provide a stronger basis for assessing the reliability of self-assembled SERS platforms for online biofluid monitoring.

Author Contributions: Conceptualization, H.C., X.Z., G.Z. and Y.M.; investigation, H.C.; writing—original draft preparation, H.C.; writing—review and editing, H.C., X.Z., G.Z., T.M. and Y.M.; visualization, H.C.; supervision, G.Z., T.M. and Y.M.; project administration, G.Z. and Y.M.; funding acquisition, G.Z. and Y.M. All authors have read and agreed to the published version of the manuscript.

Funding: This research was funded by the Beijing Natural Science Foundation, grant number L2606041, and the Project of Cultivation for Young Top-Notch Talents of Beijing Municipal Institutions, grant number BPHR202203229.

Institutional Review Board Statement: Not applicable.

Informed Consent Statement: Not applicable.

Data Availability Statement: No new data were created or analyzed in this study. Data sharing is not applicable to this article.

Acknowledgments: The authors thank Zixiao Wang for helpful discussions and suggestions during manuscript preparation.

Conflicts of Interest: The authors declare no conflicts of interest.

References

1. Kim, J.; Campbell, A.S.; De Ávila, B.E.-F.; Wang, J. Wearable Biosensors for Healthcare Monitoring. *Nat. Biotechnol.* **2019**, *37*, 389–406. [CrossRef] [PubMed]
2. Sempionatto, J.R.; Lasalde-Ramírez, J.A.; Mahato, K.; Wang, J.; Gao, W. Wearable Chemical Sensors for Biomarker Discovery in the Omics Era. *Nat. Rev. Chem.* **2022**, *6*, 899–915. [CrossRef] [PubMed]
3. Ates, H.C.; Nguyen, P.Q.; Gonzalez-Macia, L.; Morales-Narváez, E.; Güder, F.; Collins, J.J.; Dincer, C. End-to-End Design of Wearable Sensors. *Nat. Rev. Mater.* **2022**, *7*, 887–907. [CrossRef] [PubMed]
4. Heikenfeld, J.; Jajack, A.; Rogers, J.; Gutruf, P.; Tian, L.; Pan, T.; Li, R.; Khine, M.; Kim, J.; Wang, J.; et al. Wearable Sensors: Modalities, Challenges, and Prospects. *Lab Chip* **2018**, *18*, 217–248. [CrossRef] [PubMed]
5. Chen, S.; Qiao, Z.; Niu, Y.; Yeo, J.C.; Liu, Y.; Qi, J.; Fan, S.; Liu, X.; Lee, J.Y.; Lim, C.T. Wearable Flexible Microfluidic Sensing Technologies. *Nat. Rev. Bioeng.* **2023**, *1*, 950–971. [CrossRef]
6. Park, H.; Park, W.; Lee, C.H. Electrochemically Active Materials and Wearable Biosensors for the in Situ Analysis of Body Fluids for Human Healthcare. *NPG Asia Mater.* **2021**, *13*, 23. [CrossRef]
7. Wu, Z.; Qiao, Z.; Chen, S.; Fan, S.; Liu, Y.; Qi, J.; Lim, C.T. Interstitial Fluid-Based Wearable Biosensors for Minimally Invasive Healthcare and Biomedical Applications. *Commun. Mater.* **2024**, *5*, 33. [CrossRef]
8. Bai, W.; Yu, X.; Li, Q.; Tan, H.; Ma, K.; Bai, H.; Li, S.; Hu, J.; Yao, Y.; Zhuang, W.; et al. Recent Advances in the Study of Tear Biomarkers and Contact Lens-Based Biosensors. *Chem. Eng. J.* **2024**, *499*, 156540. [CrossRef]
9. Czopinska, J.; Zaras, I.; Jarczewska, M. Wearable (Bio)Sensors for Wound Healing Monitoring: Recent Achievements, Challenges, and Future Directions. *Bioelectrochemistry* **2026**, *169*, 109204. [CrossRef] [PubMed]
10. Gao, F.; Liu, C.; Zhang, L.; Liu, T.; Wang, Z.; Song, Z.; Cai, H.; Fang, Z.; Chen, J.; Wang, J.; et al. Wearable and Flexible Electrochemical Sensors for Sweat Analysis: A Review. *Microsyst. Nanoeng.* **2023**, *9*, 1. [CrossRef] [PubMed]
11. Wang, J.; Luo, Y.; Zhou, Z.; Xiao, J.; Xu, T.; Zhang, X. Epidermal Wearable Optical Sensors for Sweat Monitoring. *Commun. Mater.* **2024**, *5*, 77. [CrossRef]
12. Min, J.; Tu, J.; Xu, C.; Lukas, H.; Shin, S.; Yang, Y.; Solomon, S.A.; Mukasa, D.; Gao, W. Skin-Interfaced Wearable Sweat Sensors for Precision Medicine. *Chem. Rev.* **2023**, *123*, 5049–5138. [CrossRef] [PubMed]
13. Wang, Y.; Zhao, C.; Wang, J.; Luo, X.; Xie, L.; Zhan, S.; Kim, J.; Wang, X.; Liu, X.; Ying, Y. Wearable Plasmonic-Metasurface Sensor for Noninvasive and Universal Molecular Fingerprint Detection on Biointerfaces. *Sci. Adv.* **2021**, *7*, eabe4553. [CrossRef] [PubMed]
14. Cialla-May, D.; Bonifacio, A.; Bocklitz, T.; Markin, A.; Markina, N.; Fornasaro, S.; Dwivedi, A.; Dib, T.; Farnesi, E.; Liu, C.; et al. Biomedical SERS—The Current State and Future Trends. *Chem. Soc. Rev.* **2024**, *53*, 8957–8979. [CrossRef] [PubMed]
15. Schlücker, S. Surface-Enhanced Raman Spectroscopy: Concepts and Chemical Applications. *Angew. Chem. Int. Ed.* **2014**, *53*, 4756–4795. [CrossRef] [PubMed]
16. Ma, H.; Pan, S.-Q.; Wang, W.-L.; Yue, X.; Xi, X.-H.; Yan, S.; Wu, D.-Y.; Wang, X.; Liu, G.; Ren, B. Surface-Enhanced Raman Spectroscopy: Current Understanding, Challenges, and Opportunities. *ACS Nano* **2024**, *18*, 14000–14019. [CrossRef] [PubMed]
17. Yi, J.; You, E.-M.; Hu, R.; Wu, D.-Y.; Liu, G.-K.; Yang, Z.-L.; Zhang, H.; Gu, Y.; Wang, Y.-H.; Wang, X.; et al. Surface-Enhanced Raman Spectroscopy: A Half-Century Historical Perspective. *Chem. Soc. Rev.* **2025**, *54*, 1453–1551. [CrossRef] [PubMed]
18. Lin, L.L.; Alvarez-Puebla, R.; Liz-Marzán, L.M.; Trau, M.; Wang, J.; Fabris, L.; Wang, X.; Liu, G.; Xu, S.; Han, X.X.; et al. Surface-Enhanced Raman Spectroscopy for Biomedical Applications: Recent Advances and Future Challenges. *ACS Appl. Mater. Interfaces* **2025**, *17*, 16287–16379. [CrossRef] [PubMed]
19. Kaushik, A.; Senapati, S.; Agrawal, N.; Ali, S.A.; Habib, S.; Singh, J.P. Portable SERS for Salivary-Based Detection of Oral Pre-Malignant Lesions and Carcinomas: A Step toward Clinical Implementation. *Spectrochim. Acta Part A Mol. Biomol. Spectrosc.* **2025**, *339*, 126298. [CrossRef] [PubMed]
20. Hu, D.; Xu, X.; Zhao, Z.; Li, C.; Tian, Y.; Liu, Q.; Shao, B.; Chen, S.; Zhao, Y.; Li, L.; et al. Detecting Urine Metabolites of Bladder Cancer by Surface-Enhanced Raman Spectroscopy. *Spectrochim. Acta Part A Mol. Biomol. Spectrosc.* **2021**, *247*, 119108. [CrossRef] [PubMed]

21. Kotanen, C.N.; Martinez, L.; Alvarez, R.; Simecek, J.W. Surface Enhanced Raman Scattering Spectroscopy for Detection and Identification of Microbial Pathogens Isolated from Human Serum. *Sens. Bio-Sens. Res.* **2016**, *8*, 20–26. [CrossRef]
22. Ma, H.; Sun, X.; Chen, L.; Han, X.X.; Zhao, B.; Lu, H.; He, C. Antibody-Free Discrimination of Protein Biomarkers in Human Serum Based on Surface-Enhanced Raman Spectroscopy. *Anal. Chem.* **2018**, *90*, 12342–12346. [CrossRef] [PubMed]
23. Premasiri, W.R.; Lee, J.C.; Ziegler, L.D. Surface-Enhanced Raman Scattering of Whole Human Blood, Blood Plasma, and Red Blood Cells: Cellular Processes and Bioanalytical Sensing. *J. Phys. Chem. B* **2012**, *116*, 9376–9386. [CrossRef] [PubMed]
24. Sun, F.; Hung, H.-C.; Sinclair, A.; Zhang, P.; Bai, T.; Galvan, D.D.; Jain, P.; Li, B.; Jiang, S.; Yu, Q. Hierarchical Zwitterionic Modification of a SERS Substrate Enables Real-Time Drug Monitoring in Blood Plasma. *Nat. Commun.* **2016**, *7*, 13437. [CrossRef] [PubMed]
25. Bonifacio, A.; Cervo, S.; Sergo, V. Label-Free Surface-Enhanced Raman Spectroscopy of Biofluids: Fundamental Aspects and Diagnostic Applications. *Anal. Bioanal. Chem.* **2015**, *407*, 8265–8277. [CrossRef] [PubMed]
26. Liu, H.; He, Y.; Cao, K. Flexible Surface-Enhanced Raman Scattering Substrates: A Review on Constructions, Applications, and Challenges. *Adv. Mater. Interfaces* **2021**, *8*, 2100982. [CrossRef]
27. Li, Z.; Huang, X.; Lu, G. Recent Developments of Flexible and Transparent SERS Substrates. *J. Mater. Chem. C* **2020**, *8*, 3956–3969. [CrossRef]
28. Eom, S.-J.; Seo, H.-S.; Devaraj, V.; Lee, J.-M. Wafer-Scale, Simple, and Low-Cost Fabrication of Uniform SERS Substrates: A Review and Perspective. *Curr. Appl. Phys.* **2026**, *88*, 36–43. [CrossRef]
29. Srivastava, K.; Le-The, H.; Lozeman, J.J.A.; Van Den Berg, A.; Van Der Stam, W.; Odijk, M. Prospects of Nano-Lithographic Tools for the Fabrication of Surface-Enhanced Raman Spectroscopy (SERS) Substrates. *Micro Nano Eng.* **2024**, *23*, 100267. [CrossRef]
30. Jing, T.; Gao, R.; Zhan, C.; Yu, Y.; Chen, X.; Lu, Y.; Nam, H.K.; Kim, Y.-J.; Yu, L. Flexible Surface-Enhanced Raman Scattering Substrates: A Review on Design Strategies, Fabrication Technologies, and Applications. *Coord. Chem. Rev.* **2025**, *539*, 216739. [CrossRef]
31. Zhu, Q.; Zhao, X.; Zhang, X.; Zhu, A.; Gao, R.; Zhang, Y.; Wang, Y.; Chen, L. Au Nanocone Array with 3D Hotspots for Biomarker Chips. *CrystEngComm* **2020**, *22*, 5191–5199. [CrossRef]
32. Caldwell, J.D.; Glembocki, O.; Bezares, F.J.; Bassim, N.D.; Rendell, R.W.; Feygelson, M.; Ukaegbu, M.; Kasica, R.; Shirey, L.; Hosten, C. Plasmonic Nanopillar Arrays for Large-Area, High-Enhancement Surface-Enhanced Raman Scattering Sensors. *ACS Nano* **2011**, *5*, 4046–4055. [CrossRef] [PubMed]
33. Yu, Q.; Guan, P.; Qin, D.; Golden, G.; Wallace, P.M. Inverted Size-Dependence of Surface-Enhanced Raman Scattering on Gold Nanohole and Nanodisk Arrays. *Nano Lett.* **2008**, *8*, 1923–1928. [CrossRef] [PubMed]
34. Lin, T.-H.; Linn, N.C.; Tarajano, L.; Jiang, B.; Jiang, P. Electrochemical SERS at Periodic Metallic Nanopyramid Arrays. *J. Phys. Chem. C* **2009**, *113*, 1367–1372. [CrossRef]
35. Jambhulkar, S.; Ravichandran, D.; Zhu, Y.; Thippanna, V.; Ramanathan, A.; Patil, D.; Fonseca, N.; Thummalapalli, S.V.; Sundaravadivelan, B.; Sun, A.; et al. Nanoparticle Assembly: From Self-Organization to Controlled Micropatterning for Enhanced Functionalities. *Small* **2024**, *20*, 2306394. [CrossRef] [PubMed]
36. Zhao, L.; Fan, J.; Gong, C.; Dyke, A.; Gao, W.; Li, B. A Critical Review on Recent Progress of Solution-Processed Monolayer Assembly of Nanomaterials and Applications. *Small* **2025**, *21*, 2312268. [CrossRef] [PubMed]
37. Whitesides, G.M.; Grzybowski, B. Self-Assembly at All Scales. *Science* **2002**, *295*, 2418–2421. [CrossRef] [PubMed]
38. Grzelczak, M.; Vermant, J.; Furst, E.M.; Liz-Marzán, L.M. Directed Self-Assembly of Nanoparticles. *ACS Nano* **2010**, *4*, 3591–3605. [CrossRef] [PubMed]
39. Ye, Z.; Li, C.; Chen, Q.; Xu, Y.; Bell, S.E.J. Self-Assembly of Colloidal Nanoparticles into 2D Arrays at Water–Oil Interfaces: Rational Construction of Stable SERS Substrates with Accessible Enhancing Surfaces and Tailored Plasmonic Response. *Nanoscale* **2021**, *13*, 5937–5953. [CrossRef] [PubMed]
40. Hou, S.; Bai, L.; Lu, D.; Duan, H. Interfacial Colloidal Self-Assembly for Functional Materials. *Acc. Chem. Res.* **2023**, *56*, 740–751. [CrossRef] [PubMed]
41. Li, W.; Zhang, C.; Wang, Y. Evaporative Self-Assembly in Colloidal Droplets: Emergence of Ordered Structures from Complex Fluids. *Adv. Colloid Interface Sci.* **2024**, *333*, 103286. [CrossRef] [PubMed]
42. Scarabelli, L.; Vila-Liarte, D.; Mihi, A.; Liz-Marzán, L.M. Templated Colloidal Self-Assembly for Lattice Plasmon Engineering. *Acc. Mater. Res.* **2021**, *2*, 816–827. [CrossRef]
43. Liu, R.; Li, S.; Liu, J.-F. Self-Assembly of Plasmonic Nanostructures into Superlattices for Surface-Enhanced Raman Scattering Applications. *TrAC Trends Anal. Chem.* **2017**, *97*, 188–200. [CrossRef]
44. Zhao, Y.; Shi, L.; Tian, Y.; Zhang, L. Self-Assembly at Liquid-Liquid Interface: A New SERS Substrate for Analytical Sensing. *Chin. J. Chem.* **2023**, *41*, 569–580. [CrossRef]
45. Xu, Y.; Konrad, M.P.; Lee, W.W.Y.; Ye, Z.; Bell, S.E.J. A Method for Promoting Assembly of Metallic and Nonmetallic Nanoparticles into Interfacial Monolayer Films. *Nano Lett.* **2016**, *16*, 5255–5260. [CrossRef] [PubMed]

46. Liu, J.; Zhang, S.; Qi, H.; Wen, W.; Yu, S. A General Strategy for Self-Assembly of Nanosized Building Blocks on Liquid/Liquid Interfaces. *Small* **2012**, *8*, 2412–2420. [CrossRef] [PubMed]
47. Zhong, L.-B.; Yin, J.; Zheng, Y.-M.; Liu, Q.; Cheng, X.-X.; Luo, F.-H. Self-Assembly of Au Nanoparticles on PMMA Template as Flexible, Transparent, and Highly Active SERS Substrates. *Anal. Chem.* **2014**, *86*, 6262–6267. [CrossRef] [PubMed]
48. Sun, B.; Chen, H.; Zhang, H.; Huo, W.; Zhang, Z. Transparent and Stretchable SERS Substrates via Interfacial Transfer Self-Assembly for in-Situ Trace Thiram Fungicide Residues Detection in Fruits. *Food Chem.* **2025**, *496*, 146598. [CrossRef] [PubMed]
49. Li, L.; Chin, W.S. Rapid Fabrication of a Flexible and Transparent Ag Nanocubes@PDMS Film as a SERS Substrate with High Performance. *ACS Appl. Mater. Interfaces* **2020**, *12*, 37538–37548. [CrossRef] [PubMed]
50. Peng, R.; Zhang, T.; Wang, S.; Liu, Z.; Pan, P.; Xu, X.; Song, Y.; Liu, X.; Yan, S.; Wang, J. Self-Assembly of Strain-Adaptable Surface-Enhanced Raman Scattering Substrate on Polydimethylsiloxane Nanowrinkles. *Anal. Chem.* **2024**, *96*, 10620–10629. [CrossRef] [PubMed]
51. Pieranski, P. Two-Dimensional Interfacial Colloidal Crystals. *Phys. Rev. Lett.* **1980**, *45*, 569–572. [CrossRef]
52. Hu, J.; Zhao, B.; Xu, W.; Fan, Y.; Li, B.; Ozaki, Y. Aggregation of Silver Particles Trapped at an Air−Water Interface for Preparing New SERS Active Substrates. *J. Phys. Chem. B* **2002**, *106*, 6500–6506. [CrossRef]
53. Lin, G.; Zhou, X.; Lei, L. Mechanistic Understanding of Nanoparticle Interactions to Achieve Highly-Ordered Arrays through Self-Assembly for Sensitive Surface-Enhanced Raman Scattering Detection of Trace Thiram. *Food Chem.* **2024**, *455*, 139852. [CrossRef] [PubMed]
54. Wen, T.; Majetich, S.A. Ultra-Large-Area Self-Assembled Monolayers of Nanoparticles. *ACS Nano* **2011**, *5*, 8868–8876. [CrossRef] [PubMed]
55. Guo, Q.; Xu, M.; Yuan, Y.; Gu, R.; Yao, J. Self-Assembled Large-Scale Monolayer of Au Nanoparticles at the Air/Water Interface Used as a SERS Substrate. *Langmuir* **2016**, *32*, 4530–4537. [CrossRef] [PubMed]
56. Tian, X.-D.; Zhang, Y. Tunable Orientation of Two-Dimensional Assembled Au Octahedron Superlattices in Polymer Films as Flexible SERS Substrates. *Nanoscale* **2023**, *15*, 4317–4324. [CrossRef] [PubMed]
57. Rourke-Funderburg, A.S.; Walter, A.B.; Carroll, B.; Mahadevan-Jansen, A.; Locke, A.K. Development of a Low-Cost Paper-Based Platform for Coffee Ring-Assisted SERS. *ACS Omega* **2023**, *8*, 33745–33754. [CrossRef] [PubMed]
58. Farcau, C.; Potara, M.; Leordean, C.; Boca, S.; Astilean, S. Reliable Plasmonic Substrates for Bioanalytical SERS Applications Easily Prepared by Convective Assembly of Gold Nanocolloids. *Analyst* **2013**, *138*, 546–552. [CrossRef] [PubMed]
59. Liu, Y.; Huang, Z.; Zhou, F.; Lei, X.; Yao, B.; Meng, G.; Mao, Q. Highly Sensitive Fibre Surface-Enhanced Raman Scattering Probes Fabricated Using Laser-Induced Self-Assembly in a Meniscus. *Nanoscale* **2016**, *8*, 10607–10614. [CrossRef] [PubMed]
60. Liu, Y.; Liu, R.; Ai, C.; Wang, B.; Chu, R.; Wang, H.; Shui, L.; Zhou, F. Stick-Slip-Motion-Assisted Interfacial Self-Assembly of Noble Metal Nanoparticles on Tapered Optical Fiber Surface and Its Application in SERS Detection. *Appl. Surf. Sci.* **2022**, *602*, 154298. [CrossRef]
61. Kang, T.; Cho, Y.; Yuk, K.M.; Yu, C.Y.; Choi, S.H.; Byun, K.M. Fabrication and Characterization of Novel Silk Fiber-Optic SERS Sensor with Uniform Assembly of Gold Nanoparticles. *Sensors* **2022**, *22*, 9012. [CrossRef] [PubMed]
62. Tan, Y.; Yang, K.; Zhang, X.; Zhou, Z.; Xu, Y.; Xie, A.; Xue, C. Stretchable and Flexible Micro–Nano Substrates for SERS Detection of Organic Dyes. *ACS Omega* **2023**, *8*, 14541–14548. [CrossRef] [PubMed]
63. Hossain, M.K.; Willmott, G.R.; Etchegoin, P.G.; Blaikie, R.J.; Tallon, J.L. Tunable SERS Using Gold Nanoaggregates on an Elastomeric Substrate. *Nanoscale* **2013**, *5*, 8945. [CrossRef] [PubMed]
64. Yin, Y.; Lu, Y.; Gates, B.; Xia, Y. Template-Assisted Self-Assembly: A Practical Route to Complex Aggregates of Monodispersed Colloids with Well-Defined Sizes, Shapes, and Structures. *J. Am. Chem. Soc.* **2001**, *123*, 8718–8729. [CrossRef] [PubMed]
65. Zhai, B.; Tang, J.; Liu, J.; Wang, H.; Liu, K.; Peng, J.; Fang, Y. Towards a Scalable and Controllable Preparation of Highly-Uniform Surface-Enhanced Raman Scattering Substrates: Defect-Free Nanofilms as Templates. *J. Colloid Interface Sci.* **2023**, *647*, 23–31. [CrossRef] [PubMed]
66. Matricardi, C.; Hanske, C.; Garcia-Pomar, J.L.; Langer, J.; Mihi, A.; Liz-Marzán, L.M. Gold Nanoparticle Plasmonic Superlattices as Surface-Enhanced Raman Spectroscopy Substrates. *ACS Nano* **2018**, *12*, 8531–8539. [CrossRef] [PubMed]
67. Garg, A.; Nam, W.; Zhou, W. Reusable Surface-Enhanced Raman Spectroscopy Membranes and Textiles via Template-Assisted Self-Assembly and Micro/Nanoimprinting. *ACS Appl. Mater. Interfaces* **2020**, *12*, 56290–56299. [CrossRef] [PubMed]
68. Laghrissi, A.; Gupta, P.; Rubahn, H.-G.; Fiutowski, J. Rapid Template-Assisted Self-Assembly: A Practical Route to the Fast Assembly of Colloidal Particles. *J. Nanoparticle Res.* **2023**, *25*, 103. [CrossRef]
69. Charconnet, M.; Kuttner, C.; Plou, J.; García-Pomar, J.L.; Mihi, A.; Liz-Marzán, L.M.; Seifert, A. Mechanically Tunable Lattice-Plasmon Resonances by Templated Self-Assembled Superlattices for Multi-Wavelength Surface-Enhanced Raman Spectroscopy. *Small Methods* **2021**, *5*, 2100453. [CrossRef] [PubMed]
70. Li, J.; Cui, X.; Yang, X.; Qiu, Y.; Li, Y.; Cao, H.; Wang, D.; He, W.; Feng, Y.; Yang, Z. Quantification of Uric Acid Concentration in Tears by Using PDMS Inverse Opal Structure Surface-Enhanced Raman Scattering Substrates: Application in Hyperuricemia. *Spectrochim. Acta Part A Mol. Biomol. Spectrosc.* **2022**, *278*, 121326. [CrossRef] [PubMed]

71. Yang, W.; Li, D.; Li, Y.; Zheng, Y.; Shan, J. Synthesis of a Capillary Surface-Enhanced Raman Scattering Substrate Integrating Sampling and Detection Based on Meniscus Self-Assembled Technology. *Microchim. Acta* **2023**, *190*, 411. [CrossRef] [PubMed]
72. He, X.; Fan, C.; Luo, Y.; Xu, T.; Zhang, X. Flexible Microfluidic Nanoplasmonic Sensors for Refreshable and Portable Recognition of Sweat Biochemical Fingerprint. *npj Flex. Electron.* **2022**, *6*, 60. [CrossRef]
73. Park, M.; Chung, K.; Kim, S.; Lim, J.Y. Label-Free Surface-Enhanced Raman Spectroscopy Sensing with 3D-Printed Ag-Coated Au Nanorod Microneedles: A Langmuir–Blodgett Strategy for on-Site pH Monitoring. *Biosens. Bioelectron.* **2025**, *289*, 117848. [CrossRef] [PubMed]
74. Liu, Y.; Li, W.; Lu, Z.; Cai, H.; Yuan, R.; Yang, Y.; Qiao, X. A Microneedle-Based SERS Sensor for Simultaneous Detection of pH and Uric Acid in Interstitial Fluid. *Microchem. J.* **2026**, *222*, 117164. [CrossRef]
75. Sung, D.; Jekal, B.; Lee, S.I.; Kang, T.; Jeong, K.; Lee, S.-H.; Kwak, K.; Koo, J.; Kim, S. Quantitative Surface-Enhanced Raman Spectroscopy Analysis of Sweat Integrated with a Skin-Mounted Soft Microfluidic Reactor. *npj Flex. Electron.* **2026**, *10*, 47. [CrossRef]
76. Mogera, U.; Guo, H.; Namkoong, M.; Rahman, M.S.; Nguyen, T.; Tian, L. Wearable Plasmonic Paper–Based Microfluidics for Continuous Sweat Analysis. *Sci. Adv.* **2022**, *8*, eabn1736. [CrossRef] [PubMed]
77. Chen, Z.; Guo, Y.; Gu, X.; Liu, X.; Zhang, J.; Song, C.; Wang, L. Flexible Plasmonic Microneedle Array-Based SERS Sensor for pH Monitoring of Skin Interstitial Fluid. *Microchem. J.* **2024**, *206*, 111546. [CrossRef]
78. Narasimhan, V.; Siddique, R.H.; Park, H.; Choo, H. Bioinspired Disordered Flexible Metasurfaces for Human Tear Analysis Using Broadband Surface-Enhanced Raman Scattering. *ACS Omega* **2020**, *5*, 12915–12922. [CrossRef] [PubMed]
79. Chen, M.; Liu, G.; Wang, L.; Zhang, A.; Yang, Z.; Li, X.; Zhang, Z.; Gu, S.; Cui, D.; Haick, H.; et al. Neural Network–Enhanced Electrochemical/SERS Dual-Mode Microfluidic Platform for Accurate Detection of Interleukin-6 in Diabetic Wound Exudates. *Anal. Chem.* **2025**, *97*, 4397–4406. [CrossRef] [PubMed]
80. Gao, W.; Emaminejad, S.; Nyein, H.Y.Y.; Challa, S.; Chen, K.; Peck, A.; Fahad, H.M.; Ota, H.; Shiraki, H.; Kiriya, D.; et al. Fully Integrated Wearable Sensor Arrays for Multiplexed in Situ Perspiration Analysis. *Nature* **2016**, *529*, 509–514. [CrossRef] [PubMed]
81. Koh, A.; Kang, D.; Xue, Y.; Lee, S.; Pielak, R.M.; Kim, J.; Hwang, T.; Min, S.; Banks, A.; Bastien, P.; et al. A Soft, Wearable Microfluidic Device for the Capture, Storage, and Colorimetric Sensing of Sweat. *Sci. Transl. Med.* **2016**, *8*, 366ra165. [CrossRef] [PubMed]
82. Emaminejad, S.; Gao, W.; Wu, E.; Davies, Z.A.; Yin Yin Nyein, H.; Challa, S.; Ryan, S.P.; Fahad, H.M.; Chen, K.; Shahpar, Z.; et al. Autonomous Sweat Extraction and Analysis Applied to Cystic Fibrosis and Glucose Monitoring Using a Fully Integrated Wearable Platform. *Proc. Natl. Acad. Sci. USA* **2017**, *114*, 4625–4630. [CrossRef] [PubMed]
83. Torrente-Rodríguez, R.M.; Tu, J.; Yang, Y.; Min, J.; Wang, M.; Song, Y.; Yu, Y.; Xu, C.; Ye, C.; IsHak, W.W.; et al. Investigation of Cortisol Dynamics in Human Sweat Using a Graphene-Based Wireless mHealth System. *Matter* **2020**, *2*, 921–937. [CrossRef] [PubMed]
84. Yang, P.; Wei, G.; Liu, A.; Huo, F.; Zhang, Z. A Review of Sampling, Energy Supply and Intelligent Monitoring for Long-Term Sweat Sensors. *npj Flex. Electron.* **2022**, *6*, 33. [CrossRef]
85. Niu, Q.; Yuan, R.; Zhan, H.; Jin, J.; Qiao, X. Janus Membrane-Based Wearable Dual-Channel SERS Sensor for Sweat Collection and Monitoring of Lactic Acid and pH Levels. *Anal. Chem.* **2025**, *97*, 6083–6091. [CrossRef] [PubMed]
86. Li, G.; Zhao, X.; Tang, X.; Yao, L.; Li, W.; Wang, J.; Liu, X.; Han, B.; Fan, X.; Qiu, T.; et al. Wearable Hydrogel SERS Chip Utilizing Plasmonic Trimers for Uric Acid Analysis in Sweat. *Nano Lett.* **2024**, *24*, 13447–13454. [CrossRef] [PubMed]
87. Xiao, J.; Wang, J.; Luo, Y.; Xu, T.; Zhang, X. Wearable Plasmonic Sweat Biosensor for Acetaminophen Drug Monitoring. *ACS Sens.* **2023**, *8*, 1766–1773. [CrossRef] [PubMed]
88. Atta, S.; Zhao, Y.; Sanchez, S.; Vo-Dinh, T. A Simple and Sensitive Wearable SERS Sensor Utilizing Plasmonic-Active Gold Nanostars. *ACS Omega* **2024**, *9*, 38897–38905. [CrossRef] [PubMed]
89. Liu, C.; Xu, T.; Wang, D.; Zhang, X. The Role of Sampling in Wearable Sweat Sensors. *Talanta* **2020**, *212*, 120801. [CrossRef] [PubMed]
90. Shin, S.; Gao, W. Making Sweat Measurable: Induction, Sampling, and Refreshment in Wearable Biofluid Sensing. *Adv. Sci.* **2026**, e75684. [CrossRef] [PubMed]
91. Ursem, R.F.R.; Steijlen, A.; Parrilla, M.; Bastemeijer, J.; Bossche, A.; De Wael, K. Worth Your Sweat: Wearable Microfluidic Flow Rate Sensors for Meaningful Sweat Analytics. *Lab Chip* **2025**, *25*, 1296–1315. [CrossRef] [PubMed]
92. Hu, M.; Zhu, K.; Wei, J.; Yang, K.; Wu, L.; Zong, S.; Wang, Z. Silk Fibroin-Based Wearable SERS Biosensor for Simultaneous Sweat Monitoring of Creatinine and Uric Acid. *Biosens. Bioelectron.* **2024**, *265*, 116662. [CrossRef] [PubMed]
93. Hu, M.; Zhu, K.; Wei, J.; Xu, Z.; Yang, K.; Wu, L.; Zong, S.; Wang, Z. Wearable Microfluidic SERS Patch Based on Silk Fibroin for the Non-Invasive Monitoring of Sweat Cortisol and pH. *Sens. Actuators B Chem.* **2025**, *427*, 137152. [CrossRef]
94. Zhu, J.; Yu, W.; Xiong, H.; Xia, X.; Li, Y.; Huang, Y. Wearable Double Network Plasmonic Hydrogel for SERS Detection of Urea and Uric Acid in Sweat. *ACS Sens.* **2025**, *10*, 6123–6131. [CrossRef] [PubMed]

95. Ye, H.; Chen, X.; Huang, X.; Li, C.; Yin, X.; Zhao, W.; Wang, T. Patterned Gold Nanoparticle Superlattice Film for Wearable Sweat Sensors. *Nano Lett.* **2024**, *24*, 11082–11089. [CrossRef] [PubMed]
96. Pan, S.; Tian, X.; Lu, Y.; Liao, Y.; Liu, M.; Meng, L.; Zhou, L.; Zhang, Y. Wearable SERS-Microfluidic Patch for Real-Time in Situ Monitoring of Chiral Metabolites in Sweat. *Small* **2025**, *21*, 2500770. [CrossRef] [PubMed]
97. Shi, S.; Wang, Y.; Mei, R.; Zhao, X.; Liu, X.; Chen, L. Revealing Drug Release and Diffusion Behavior in Skin Interstitial Fluid by Surface-Enhanced Raman Scattering Microneedles. *J. Mater. Chem. B* **2023**, *11*, 3097–3105. [CrossRef] [PubMed]
98. Li, D.; Zhao, S.; Zhang, W.; Li, Y.; Masaki, T.; Ma, G.; Peng, Y.; Yang, Y. Ion-Induced Plasmonic Microneedle Patches for Ultrasensitive SERS Detection Hemoporfin in Interstitial Fluids. *Biosens. Bioelectron.* **2026**, *308*, 118778. [CrossRef] [PubMed]
99. Zhang, X.; Zhang, W.; Wu, W.; Chen, J. Recent Advances in the Preparation of Microneedle Patches for Interstitial Fluid Extraction and Analysis. *Microchem. J.* **2023**, *195*, 109477. [CrossRef]
100. Gu, Z.; Zhao, D.; He, H.; Wang, Z. SERS-Based Microneedle Biosensor for In Situ and Sensitive Detection of Tyrosinase. *Biosensors* **2024**, *14*, 202. [CrossRef] [PubMed]
101. Chia, Z.-C.; Chen, Y.-L.; Chuang, C.-H.; Hsieh, C.-H.; Chen, Y.-J.; Chen, K.-H.; Huang, T.-C.; Chen, M.-C.; Huang, C.-C. Polyphenol-Assisted Assembly of Au-Deposited Polylactic Acid Microneedles for SERS Sensing and Antibacterial Photodynamic Therapy. *Chem. Commun.* **2023**, *59*, 6339–6342. [CrossRef] [PubMed]
102. Park, J.E.; Yonet-Tanyeri, N.; Vander Ende, E.; Henry, A.-I.; Perez White, B.E.; Mrksich, M.; Van Duyne, R.P. Plasmonic Microneedle Arrays for in Situ Sensing with Surface-Enhanced Raman Spectroscopy (SERS). *Nano Lett.* **2019**, *19*, 6862–6868. [CrossRef] [PubMed]
103. Kolluru, C.; Gupta, R.; Jiang, Q.; Williams, M.; Gholami Derami, H.; Cao, S.; Noel, R.K.; Singamaneni, S.; Prausnitz, M.R. Plasmonic Paper Microneedle Patch for On-Patch Detection of Molecules in Dermal Interstitial Fluid. *ACS Sens.* **2019**, *4*, 1569–1576. [CrossRef] [PubMed]
104. Tehrani, F.; Teymourian, H.; Wuerstle, B.; Kavner, J.; Patel, R.; Furmidge, A.; Aghavali, R.; Hosseini-Toudeshki, H.; Brown, C.; Zhang, F.; et al. An Integrated Wearable Microneedle Array for the Continuous Monitoring of Multiple Biomarkers in Interstitial Fluid. *Nat. Biomed. Eng.* **2022**, *6*, 1214–1224. [CrossRef] [PubMed]
105. Li, B.; Sheng, M.; Xie, L.; Liu, F.; Yan, G.; Wang, W.; Lin, A.; Zhao, F.; Chen, Y. Tear Proteomic Analysis of Patients with Type 2 Diabetes and Dry Eye Syndrome by Two-Dimensional Nano-Liquid Chromatography Coupled with Tandem Mass Spectrometry. *Investig. Ophthalmol. Vis. Sci.* **2014**, *55*, 177–186. [CrossRef] [PubMed]
106. Zhao, W.; Li, J.; Xue, Z.; Qiao, X.; Li, A.; Chen, X.; Feng, Y.; Yang, Z.; Wang, T. A Separation-Sensing Platform Performing Accurate Diagnosis of Jaundice in Complex Biological Tear Fluids. *Angew. Chem. Int. Ed.* **2022**, *61*, e202205628. [CrossRef] [PubMed]
107. Kim, S.; Kim, T.G.; Lee, S.H.; Kim, W.; Bang, A.; Moon, S.W.; Song, J.; Shin, J.-H.; Yu, J.S.; Choi, S. Label-Free Surface-Enhanced Raman Spectroscopy Biosensor for On-Site Breast Cancer Detection Using Human Tears. *ACS Appl. Mater. Interfaces* **2020**, *12*, 7897–7904. [CrossRef] [PubMed]
108. Park, W.; Seo, H.; Kim, J.; Hong, Y.-M.; Song, H.; Joo, B.J.; Kim, S.; Kim, E.; Yae, C.-G.; Kim, J.; et al. In-Depth Correlation Analysis between Tear Glucose and Blood Glucose Using a Wireless Smart Contact Lens. *Nat. Commun.* **2024**, *15*, 2828. [CrossRef] [PubMed]
109. Han, M.; Silva, S.M.; Russo, M.J.; Desroches, P.E.; Lei, W.; Quigley, A.F.; Kapsa, R.M.I.; Moulton, S.E.; Stoddart, P.R.; Greene, G.W. Lubricin (PRG-4) Anti-Fouling Coating for Surface-Enhanced Raman Spectroscopy Biosensing: Towards a Hierarchical Separation System for Analysis of Biofluids. *Analyst* **2024**, *149*, 63–75. [CrossRef] [PubMed]
110. Cui, X.; Li, J.; Li, Y.; Liu, M.; Qiao, J.; Wang, D.; Cao, H.; He, W.; Feng, Y.; Yang, Z. Detection of Glucose in Diabetic Tears by Using Gold Nanoparticles and MXene Composite Surface-Enhanced Raman Scattering Substrates. *Spectrochim. Acta Part A Mol. Biomol. Spectrosc.* **2022**, *266*, 120432. [CrossRef] [PubMed]
111. Goto, T.; Saligan, L.N. Wound Pain and Wound Healing Biomarkers From Wound Exudate: A Scoping Review. *J. Wound Ostomy Cont. Nurs.* **2020**, *47*, 559–568. [CrossRef] [PubMed]
112. Zhou, Y.; Zhang, W.; Cheng, S.; Xing, Y.; Wang, J.; Yu, F.; Wang, R. Flexible PDMS-SERS Platform for Culture-Free Diagnosis of Bacterial Infections in Clinical Wound Care. *Talanta* **2025**, *293*, 128089. [CrossRef] [PubMed]
113. Guo, J.; Zhong, Z.; Li, Y.; Liu, Y.; Wang, R.; Ju, H. "Three-in-One" SERS Adhesive Tape for Rapid Sampling, Release, and Detection of Wound Infectious Pathogens. *ACS Appl. Mater. Interfaces* **2019**, *11*, 36399–36408. [CrossRef] [PubMed]
114. Bodelón, G.; Montes-García, V.; López-Puente, V.; Hill, E.H.; Hamon, C.; Sanz-Ortiz, M.N.; Rodal-Cedeira, S.; Costas, C.; Celiksoy, S.; Pérez-Juste, I.; et al. Detection and Imaging of Quorum Sensing in *Pseudomonas aeruginosa* Biofilm Communities by Surface-Enhanced Resonance Raman Scattering. *Nat. Mater.* **2016**, *15*, 1203–1211. [CrossRef] [PubMed]
115. Nguyen, C.Q.; Thrift, W.J.; Bhattacharjee, A.; Ranjbar, S.; Gallagher, T.; Darvishzadeh-Varcheie, M.; Sanderson, R.N.; Capolino, F.; Whiteson, K.; Baldi, P.; et al. Longitudinal Monitoring of Biofilm Formation via Robust Surface-Enhanced Raman Scattering Quantification of *Pseudomonas aeruginosa*-Produced Metabolites. *ACS Appl. Mater. Interfaces* **2018**, *10*, 12364–12373. [CrossRef] [PubMed]

116. Cao, J.; Yang, W.-T.; Cao, D.; Wu, C.-Y.; Zhou, P.-C.; Zhu, W.; Liao, S.-J.; Hu, J.-M.; Shen, A.-G.; Popp, J. Feedback-Guided SERS-Photothermal Patch for Maintaining Redox Homeostasis in Diabetic Foot Ulcers. *Anal. Chem.* **2026**, *98*, 6986–7000. [CrossRef] [PubMed]
117. Guo, Y.; Li, Y.; Fan, R.; Liu, A.; Chen, Y.; Zhong, H.; Liu, Y.; Chen, H.; Guo, Z.; Liu, Z. Silver@Prussian Blue Core–Satellite Nanostructures as Multimetal Ions Switch for Potent Zero-Background SERS Bioimaging-Guided Chronic Wound Healing. *Nano Lett.* **2023**, *23*, 8761–8769. [CrossRef] [PubMed]
118. Johnston, H.J.; Hutchison, G.; Christensen, F.M.; Peters, S.; Hankin, S.; Stone, V. A Review of the in Vivo and in Vitro Toxicity of Silver and Gold Particulates: Particle Attributes and Biological Mechanisms Responsible for the Observed Toxicity. *Crit. Rev. Toxicol.* **2010**, *40*, 328–346. [CrossRef] [PubMed]
119. Kus-Liśkiewicz, M.; Fickers, P.; Ben Tahar, I. Biocompatibility and Cytotoxicity of Gold Nanoparticles: Recent Advances in Methodologies and Regulations. *Int. J. Mol. Sci.* **2021**, *22*, 10952. [CrossRef] [PubMed]
120. Reidy, B.; Haase, A.; Luch, A.; Dawson, K.; Lynch, I. Mechanisms of Silver Nanoparticle Release, Transformation and Toxicity: A Critical Review of Current Knowledge and Recommendations for Future Studies and Applications. *Materials* **2013**, *6*, 2295–2350. [CrossRef] [PubMed]
121. Hadrup, N.; Sharma, A.K.; Loeschner, K. Toxicity of Silver Ions, Metallic Silver, and Silver Nanoparticle Materials after in Vivo Dermal and Mucosal Surface Exposure: A Review. *Regul. Toxicol. Pharmacol.* **2018**, *98*, 257–267. [CrossRef] [PubMed]
122. Lv, Y.; Qin, Y.; Svec, F.; Tan, T. Molecularly Imprinted Plasmonic Nanosensor for Selective SERS Detection of Protein Biomarkers. *Biosens. Bioelectron.* **2016**, *80*, 433–441. [CrossRef] [PubMed]
123. Ding, Y.; Sun, Y.; Liu, C.; Jiang, Q.; Chen, F.; Cao, Y. SERS-Based Biosensors Combined with Machine Learning for Medical Application. *ChemistryOpen* **2023**, *12*, e202200192. [CrossRef] [PubMed]

Disclaimer/Publisher's Note: The statements, opinions and data contained in all publications are solely those of the individual author(s) and contributor(s) and not of MDPI and/or the editor(s). MDPI and/or the editor(s) disclaim responsibility for any injury to people or property resulting from any ideas, methods, instructions or products referred to in the content.